Monthly Notices of the ROYAL ASTRONOMICAL SOCIETY

MNRAS **530,** 966–983 (2024) https://doi.org/10.1093/mnras/stae754
Advance Access publication 2024 March 15

Unveiling the hidden Universe with *JWST*: the contribution of dust-obscured galaxies to the stellar mass function at $z \sim 3 - 8$

R. Gottumukkala [1,2,3]★ L. Barrufet [1,4] P. A. Oesch [1,2,3] A. Weibel,[1] N. Allen [2,3] B. Alcalde Pampliega [5] E. J. Nelson [6] C. C. Williams [7,8] G. Brammer [2,3] Y. Fudamoto [9,10] V. González [11] K. E. Heintz [2,3] G. Illingworth [12] D. Magee [12] R. P. Naidu [13]† M. Shuntov [2,3] M. Stefanon [14,15] S. Toft [2,3] F. Valentino [2,3,16] and M. Xiao [1]

[1]*Department of Astronomy, University of Geneva, Chemin Pegasi 51, CH-1290 Versoix, Switzerland*
[2]*Cosmic Dawn Center (DAWN)*
[3]*Niels Bohr Institute, University of Copenhagen, Jagtvej 128, DK-2200, Copenhagen N, Denmark*
[4]*Institute for Astronomy, School of Physics & Astronomy, University of Edinburgh, Royal Observatory, Edinburgh EH9 3HJ, UK*
[5]*European Southern Observatory, Alonso de Córdova 3107, Vitacura, Santiago, Región Metropolitana, 7630355, Chile*
[6]*Department for Astrophysical and Planetary Science, University of Colorado, Boulder, CO 80309, USA*
[7]*NSF's National Optical-Infrared Astronomy Research Laboratory, 950 North Cherry Avenue, Tucson, AZ 85719, USA*
[8]*Steward Observatory, University of Arizona, 933 N. Cherry Avenue, Tucson, 85721, USA*
[9]*Waseda Research Institute for Science and Engineering, Faculty of Science and Engineering, Waseda University, 3-4-1 Okubo, Shinjuku, Tokyo 169-8555, Japan*
[10]*National Astronomical Observatory of Japan, 2-21-1, Osawa, Mitaka, Tokyo,181-8588, Japan*
[11]*Departamento de Astronomía, Universidad de Chile, Camino del Observatorio 1515, Las Condes, Santiago 7591245, Chile*
[12]*Department of Astronomy and Astrophysics, University of California, Santa Cruz, CA 95064, USA*
[13]*MIT Kavli Institute for Astrophysics and Space Research, 77 Massachusetts Ave., Cambridge, MA 02139, USA*
[14]*Departament d'Astronomia i Astrofísica, Universitat de València, C. Dr Moliner 50, E-46100 Burjassot, València, Spain*
[15]*Unidad Asociada CSIC "Grupo de Astrofísica Extragaláctica y Cosmologia" Instituto de Física de Cantabria - Universitat de València, 39005, Spain*
[16]*European Southern Observatory, Karl Schwarzschild Strasse 2, D-85748 Garching, Germany*

Accepted 2024 March 12. Received 2024 March 11; in original form 2023 October 5

ABSTRACT

With the advent of *JWST*, we can probe the rest-frame optical emission of galaxies at $z > 3$ with high sensitivity and spatial resolution, making it possible to accurately characterize red, optically faint galaxies and thus move towards a more complete census of the galaxy population at high redshifts. To this end, we present a sample of 148 massive, dusty galaxies from the *JWST*/Cosmic Evolution Early Release Science survey, colour-selected using solely *JWST* bands. With deep *JWST*/NIRCam data from 1.15 to 4.44 μm and ancillary *HST*/ACS and WFC3 data, we determine the physical properties of our sample using spectral energy distribution fitting with BAGPIPES. We demonstrate that our selection method efficiently identifies massive ($\langle \log M_\star/\mathrm{M}_\odot \rangle \sim 10$) and dusty ($\langle A_\mathrm{V} \rangle \sim 2.7$ mag) sources, with a majority at $z > 3$ and predominantly lying on the galaxy main sequence. The main results of this work are the stellar mass functions (SMFs) of red, optically faint galaxies from redshifts between $3 < z < 8$: these galaxies make up a significant relative fraction of the pre-*JWST* total SMF at $3 < z < 4$ and $4 < z < 6$, and dominate the high-mass end of the pre-*JWST* SMF at $6 < z < 8$, suggesting that our census of the galaxy population needs amendment at these epochs. While larger areas need to be surveyed in the future, our results suggest already that the integrated stellar mass density at $\log M_\star/\mathrm{M}_\odot \geq 9.25$ may have been underestimated in pre-*JWST* studies by up to ∼15–20% at $z \sim 3$–6, and up to ∼45% at $z \sim 6$–8, indicating the rapid onset of obscured stellar mass assembly in the early Universe.

Key words: methods: observational – techniques: photometric – galaxies: evolution – galaxies: high-redshift – infrared: galaxies.

1 INTRODUCTION

For decades, observational astronomers have been on a quest to determine how the galaxy population evolves through cosmic time. The *Hubble Space Telescope* (*HST*) has pioneered the study of this question: *HST* has observed high-redshift galaxies, primarily through their rest-frame ultraviolet (UV) emission. These high-redshift galaxies, usually referred to as 'normal' or Lyman-break galaxies (LBGs), have been studied extensively from z ∼ 3 to z ∼ 11, tending to have moderate star formation rates (SFRs) and stellar masses, and are thought to make up the bulk of the galaxy population (e.g. Labbé et al. 2013; Schaerer, de Barros & Sklias 2013; Bouwens

★ E-mail: rashmi.gottumukkala@gmail.com
† NASA Hubble Fellow.

et al. 2015; Finkelstein et al. 2015; Oesch et al. 2016; Faisst et al. 2020). These mostly dust un-obscured galaxies are also thought to dominate the cosmic star formation rate density (SFRD) at $z > 4$, while at lower redshifts the Universe was dominated by obscured star formation (e.g. Madau & Dickinson 2014; Zavala et al. 2021). While 'normal', un-obscured galaxies have been well-studied, our census of the galaxy population remains incomplete at $z > 3$ as rest-frame UV selections systematically miss massive, dust-obscured sources (e.g. Alcalde Pampliega et al. 2019; Wang et al. 2019).

Over the last decade, a significant population of optically undetected galaxies with relatively bright infrared (IR) or submillimetre (sub-mm) emission has been discovered, several in *Spitzer*/IRAC data and some of them with ALMA detections (e.g. Huang et al. 2011; Simpson et al. 2014; Caputi et al. 2015; Stefanon et al. 2015; Wang et al. 2016; Franco et al. 2018; Alcalde Pampliega et al. 2019; Wang et al. 2019; Williams et al. 2019; Yamaguchi et al. 2019; Dudzevičiūtė et al. 2020; Smail et al. 2021; Sun et al. 2021; Manning et al. 2022; Shu et al. 2022; Xiao et al. 2023b). They typically have very red spectral energy distributions (SEDs) and remain undetected even in deep *HST* H-band observations – hence their name: *HST*–dark galaxies. Their SEDs are not well-constrained, with a few photometric detections and lack of spectroscopic redshifts, which result in very large uncertainties on their photometric redshifts, stellar masses, and SFRs (e.g. Caputi et al. 2012; Stefanon et al. 2015; Alcalde Pampliega et al. 2019; Williams et al. 2019). The physical properties of these galaxies were largely unconstrained until the arrival of the *James Webb Space Telescope* (*JWST*; Gardner et al. 2023).

JWST has revolutionized the field of optically faint galaxies, providing for the first time reliable physical parameters (e.g. Barrufet et al. 2023; Gómez-Guijarro et al. 2023; Labbé et al. 2023b; Nelson et al. 2023; Pérez-González et al. 2023; Rodighiero et al. 2023). With its unprecedented sensitivity and resolution in the near-IR, *JWST* probes the rest-frame optical emission of galaxies at $z \gtrsim 3$, allowing one to identify the Balmer break, a good redshift and mass indicator. Additionally, the SEDs of massive galaxies are typically highly dust-attenuated with characteristic red slopes in the rest-frame optical. With its extensive photometric coverage from 1 to 5 μm, *JWST*'s Near-Infrared Camera (NIRCam; Rieke et al. 2023) is the ideal instrument to identify sources based on these features.

The early *JWST* era has seen the puzzling emergence of two additional populations of galaxies. The first is a population of massive sources ($> 10^{10}$ $M_\odot$) at $z > 7$, less than 700 Myr after the big bang (e.g. Labbé et al. 2023b). With the currently accepted theory of hierarchical structure formation within Lambda cold dark matter (ΛCDM) cosmology, it is challenging to explain how galaxies could accumulate this much mass through mergers or accretion alone (Menci et al. 2022; Boylan-Kolchin 2023), while it might still be possible to reconcile such observations with theory (Dekel et al. 2023; Mason, Trenti & Treu 2023). One possibility is that these sources are actually active galactic nuclei (AGNs), with one Labbé et al. (2023b) source being spectroscopically confirmed to be an AGN with broad emission lines (Kocevski et al. 2023). A deeper investigation into massive galaxies in the early Universe is needed in order to determine their abundance and place constraints on mass assembly.

The second emergent population consists of massive quiescent galaxies at high redshifts, now spectroscopically confirmed up to $z = 4.658$ (Carnall et al. 2023). Relatively little physical insight has been provided by simulations thus far to explain the emergence of quiescent galaxies at $z > 3$, with simulations struggling to predict observed number densities (Gould et al. 2023; Valentino et al. 2023). While it is highly likely that submillimetre galaxies (SMGs) evolved into massive quiescent galaxies at $z \sim 2$ (Toft et al. 2014), their number densities are insufficient to explain the presence of quiescent galaxies at $z \sim 3-4$ (Valentino et al. 2020, 2023). Hence, an important step towards understanding the emergence of quenched galaxies is to look for previously missed massive, dusty galaxies in the early Universe and determine their stellar masses and abundances.

For the study of galaxy abundances, the stellar mass function (SMF) is an extremely useful statistical tool to quantify the evolution of the galaxy population as a function of stellar mass across cosmic history. Determining the SMF at various epochs in the history of the Universe allows us to track early galaxy build-up. Several studies have so far constrained high-z SMFs with ground- and space-based multiwavelength observations (e.g. Stefanon et al. 2015; Davidzon et al. 2017; Stefanon et al. 2017b; McLeod et al. 2021; Santini et al. 2021; Stefanon et al. 2021; Navarro-Carrera et al. 2024; Weaver et al. 2023b), with the shape of the total SMF being found to be accurately described by the empirically motivated Schechter (1976) function. Given that *JWST* is primed to find massive, dust-obscured sources that have previously been missed in the galaxy census, this raises the question of whether or not the total SMF at high-z epochs requires modification. The central question we aim to address with this work is, 'How do massive, dusty galaxies selected with *JWST* affect the high-mass end of the galaxy SMF in the early Universe?'

In this study, we use data from the Cosmic Evolution Early Release Science (CEERS) survey (Finkelstein et al. 2022, 2023), a *JWST* Cycle 1 community survey in the CANDELS/Extended Groth Strip (EGS) field. CEERS is aimed at discovering the first galaxies and observing galaxy assembly at $z > 3$. Given its deep photometric coverage with *JWST*/NIRCam from 1.15 to 4.44 μm, CEERS is the ideal survey to look for red, IR-bright galaxies.

This paper is structured as follows. In Section 2, we discuss the photometric data used from *HST* and *JWST* and the production of the *HST*–*JWST* merged photometric catalogue. We introduce our colour selection using photometry solely from *JWST*. Furthermore, we describe how we create an AGN-cleaned sample of purely star-forming galaxies. In Section 3, we explain the SED fitting performed using the PYTHON tool BAGPIPES (Carnall et al. 2018). In Section 4, we discuss the physical properties of our sample, and situate our galaxies on the galaxy main sequence (MS; Section 4.3). In Section 5, we discuss the methodology used to compute the SMFs (Section 5.1) and present the SMFs of massive, dusty galaxies at $3 < z < 4$, $4 < z < 6$, and $6 < z < 8$ (Section 5.2). Finally, we discuss our sample in the context of other *JWST* studies in Section 6, and we summarize and conclude our study in Section 7.

For this work, we assume a flat ΛCDM cosmological model with $H_0 = (67.8 \pm 0.9)$ km s^{-1} Mpc^{-1} and $\Omega_m = 0.308 \pm 0.012$ as found by the Planck Collaboration XIII (2016). All magnitudes are quoted in the AB magnitude system (Oke & Gunn 1983). Throughout this paper, we use a Kroupa (2001) initial mass function (IMF). If required for comparison, we scale mass values used in the literature from Salpeter (1955) or Chabrier (2003) to Kroupa (2001) using the scale factors quoted in Madau & Dickinson (2014).

2 OBSERVATIONS AND SAMPLE SELECTION

In this section, we describe the imaging data used in this work and the production of the *HST* and *JWST* merged photometric catalogue for the CEERS field. In addition, we present our sample selection criteria in order to identify massive and dusty galaxies, including the colour-selection we develop as well as the criteria used to identify and remove AGN from our final sample.

Table 1. 5σ depths measured in 0.16 arcsec apertures in *HST*/ACS, *HST*/WFC3, and *JWST*/NIRCam photometric filters. Depths are quoted in AB magnitudes.

Telescope/Instrument	Filter	5σ depth (AB mag)
HST/ACS	*F*435*W*	28.27
	*F*606*W*	28.36
	*F*814*W*	28.19
HST/WFC3	*F*105*W*	27.96
	*F*125*W*	27.74
	*F*140*W*	26.99
	*F*160*W*	27.81
JWST/NIRCam	*F*115*W*	28.63
	*F*150*W*	28.65
	*F*200*W*	28.93
	*F*277*W*	29.17
	*F*356*W*	29.17
	*F*410*M*	28.41
	*F*444*W*	28.81

2.1 Imaging data

We use data from the CEERS programme, one of *JWST*'s first early-release science surveys in Cycle 1, with data collected in 2022 June and December (Finkelstein et al. 2022, 2023). CEERS comprises 10 NIRCam pointings covering $\sim$100 arcmin^2 in the EGS field, a CANDELS legacy field containing a wealth of ancillary *HST* multiwavelength data. The NIRCam data covers a range of wavelengths from 1.15 to 4.44 μm in the following filters: *F*115*W*, *F*150*W*, *F*200*W*, *F*277*W*, *F*356*W*, *F*410*M*, and *F*444*W* (where *W* and *M* indicate a wide or medium band filter). Ancillary *HST* data from the ACS imager is available at wavelengths between 435 and 814 nm (in three filters: *F*435*W*, *F*606*W*, and *F*814*W*) and from the WFC3 imager at wavelengths between 1.05 and 1.60 μm (in four filters: *F*105*W*, *F*125*W*, *F*140*W*, and *F*160*W*; Grogin et al. 2011; Koekemoer et al. 2011; Stefanon et al. 2017a).

For this work, we use the version five (v5) images reduced with the GRIZLI pipeline and made publicly available by G. Brammer,[1] following the same steps as outlined in Valentino et al. (2023). The images include all available data over these fields taken with *HST* and *JWST*. The imaging depths as measured in circular apertures with a radius of 0.16″are listed in Table 1. They vary between 28.6 and 29.2 mag in the *JWST* wide filters and are $\sim$ 28.3 mag in the shortest wavelength ACS imaging.

2.2 Production of the *HST–JWST* photometric catalogue

We use the *JWST* and ancillary *HST* images to create photometric catalogues, taking into account the wavelength-dependent point spread function (PSF). In the following, we briefly describe how the PSF-matched photometric catalogue used in this work was produced (see Weibel et al. 2024 for details).

We match the fluxes in all *HST* + *JWST* filters to the PSF resolution in the reddest *JWST*/NIRCam filter, *F*444*W*. For the NIRCam and WFC3 filters, we use the PSFs provided by G. Brammer for use with the CEERS GRIZLI mosaics (Brammer 2018).[2]

For the ACS filters, we derive effective PSFs from the science images by first identifying bright, but unsaturated stars without bright neighbouring sources or flagged pixels, from a preliminary SOURCEEXTRACTOR run (Bertin & Arnouts 1996). Then, we use the method `EPSFBuilder` from the PYTHON package PHOTUTILS (Bradley et al. 2022) which is based on the model developed by Anderson & King (2000) to obtain the final effective PSFs.

We compute matching kernels from each ACS and NIRCam PSF to the NIRCam/*F*444*W* PSF using the software package PYPHER (Boucaud et al. 2016) and convolve each flux and root mean square (rms) image with the respective kernel to match the PSF resolution in *F*444*W*.

We follow a different procedure for the WFC3 filters because their PSFs are broader than the NIRCam/*F*444*W* PSF. First, we compute matching kernels from all of them and from the F444W PSF to the WFC3/*F*160*W* PSF, in the same way as described above, and produce PSF-matched flux and rms images accordingly.

Then, we run SOURCEEXTRACTOR in dual mode, using an inverse-variance weighted stack of the unaltered *F*277W + *F*356*W* + *F*444*W* images as the detection image and measuring fluxes in circular apertures with a radius of 0.16″on the original images, the images that were PSF-matched to *F*444*W* as well as the images that were PSF-matched to *F*160*W*. For the final catalogue, we use the flux measurements on the original image in *F*444*W* and those on the images PSF-matched to *F*444*W* for all other filters, except the WFC3 data. For the latter, we correct the fluxes measured on the original images to match the colour between the respective filter and *F*444*W* as measured on the images PSF-matched to *F*160*W*.

We scale all fluxes to the flux measured in Kron-like apertures by SOURCEEXTRACTOR in *F*444*W*, obtained using the default Kron parameters 2.5 and 3.5. To account for residual flux outside the Kron aperture, we measure the fraction of the energy enclosed by a circular aperture with a radius of $\sqrt{a\,b}\,$`kron_radius`, where a, b and `kron_radius` characterize the Kron-ellipse, on the theoretical *F*444*W* PSF obtained from `webbpsf`, and divide all fluxes by that fraction. Finally, we correct all fluxes for Milky Way foreground extinction using the extinction model from Fitzpatrick & Massa (2007) through the PYTHON package `extinction`, using the $E(B-V)$ map outlined in Schlafly & Finkbeiner (2011).

To get a more realistic estimate of the rms uncertainty of our flux measurements that accounts for correlated noise, we put down circular apertures with a radius of 0.16 arcsec in 5000 random positions on the 'signal-to-noise' image (i.e. the flux image divided by the rms image). We multiply the uncertainties on all fluxes, measured from the rms map, respectively, by the scatter measured among those apertures. This leads to a scaling of the flux uncertainties by $\sim$5% to $\sim$35% depending on the filter – the largest correction being applied to *F*115*W* and the smallest to *F*444*W*.

To identify and flag stars, we used a flux ratio criterion similar to Weaver et al. (2023b). We also flag objects as artefacts that are too small to be real sources (typically left-over bad pixels). The full CEERS catalogue contains 93 922 sources. Out of these, we remove 930 sources that are either identified as stars or flagged as artefacts based on the above criteria, resulting finally in 92 992 sources.

2.3 Selection of red, optically dark/faint sources at $z > 3$

Over the last decade, numerous studies of *HST*-dark galaxies and red galaxies have been conducted, with dropout and colour selections shown to be effective methods for selecting high-redshift sources. Typically, these studies combine *HST* and *Spitzer* data to select massive and dusty star-forming galaxies (DSFGs; e.g. Huang et al. 2011; Alcalde Pampliega et al. 2019; Wang et al. 2019; Sun et al. 2021).

[1] https://dawn-cph.github.io/dja/
[2] https://github.com/gbrammer/grizli-psf-library

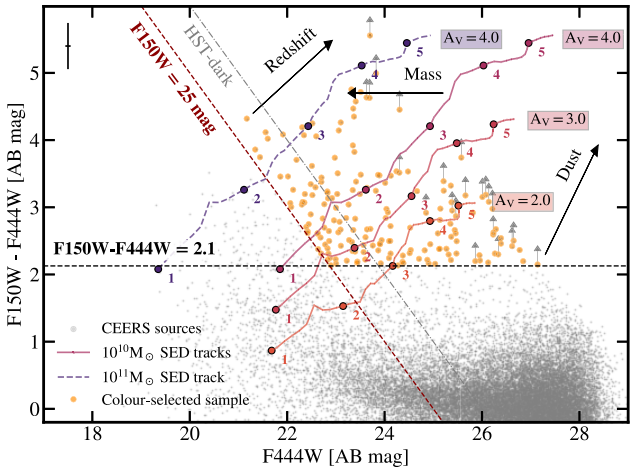

Figure 1. Colour–magnitude diagram of *F*150*W*–*F*444*W* versus *F*444*W* showing our selection method. The grey scatter points show all the sources in the CEERS catalogue, while the orange scatter points are our selected galaxies. The coloured lines are SED tracks for various dust attenuation values (A_V is indicated in boxes), with coloured numbers indicating the redshift – solid lines correspond to 10^{10} $M_\odot$ and the dashed line corresponds to 10^{11} $M_\odot$. The grey arrows show upper limits for the sources with *F*150*W* mag lower than 2σ (median errors are shown by the cross in the upper right of the figure). The colour criterion *F*150*W*–*F*444*W* > 2.1 mag (black dashed line) in principle identifies $z > 3$ sources with $A_V \gtrsim 2$ mag and $\log(M_\star/M_\odot) \sim 10$, while the magnitude cut *F*150*W* > 25 mag (dark red dashed line) is designed to rid the sample of low-z sources while retaining the most massive galaxies in the sample ($\sim 10^{11}$ $M_\odot$). Also shown for reference is the *F*150*W* = 26 mag cut that is a proxy for identifying *HST*-dark sources (Pérez-González et al. 2023). We select 179 red galaxies with these criteria that theoretically restrict our sample to massive, dusty, high-redshift galaxies.

Several unique colour cuts have been used over the last decade for efficient selections of red galaxies using *HST*/WFC3 bands in the optical and *Spitzer*/IRAC and (recently) *JWST*/NIRCam bands in the near-IR (e.g. Huang et al. 2011; Caputi et al. 2012; Wang et al. 2016; Alcalde Pampliega et al. 2019; Wang et al. 2019; Sun et al. 2021; Barrufet et al. 2023; Nelson et al. 2023; Pérez-González et al. 2023; Rodighiero et al. 2023; Long et al. 2023a; Labbé et al. 2023b; Xiao et al. 2023b). Here, we build on these and make a broad selection of red galaxies using solely *JWST*/NIRCam bands in order to fully exploit the increased sensitivity and resolution of *JWST*. By designing and implementing a colour selection capable of identifying the effects of the Balmer-break and reddened stellar continuum emission in a galaxy's photometry, we expect to select massive and dusty galaxies at high redshifts. For this, we use the PYTHON tool Bayesian Analysis of Galaxies for Physical Inference and Parameter EStimation (BAGPIPES; Carnall et al. 2018)[3] to investigate the evolution of colour with redshift. We generate galaxy spectra, from which we extract the photometry and compute modelled colours. We use a delayed-τ star formation history, ages of 1 Gyr, an e-folding time of 3 Gyr, a mass of 10^{10} $M_\odot$ and metallicity of 0.5 $Z_\odot$. We model galaxies at redshifts between $z = (1., 6.)$ in steps of $\Delta z = 0.1$ and at discrete dust attenuation values of $A_V = [2.0, 3.0, 4.0]$ mag using a Calzetti dust model (Calzetti et al. 2000) to produce the SED tracks of massive, dusty galaxies as shown by the coloured lines in Fig. 1. We also model a single SED track of a 10^{11} $M_\odot$ massive galaxy with $A_V = 4$ mag.

As the Balmer break gets redshifted beyond 1.5 μm at $z \gtrsim 3$, we design a colour cut that requires galaxies to be faint in *F*150*W* in comparison to longer wavelength bands. Pérez-González et al. (2023) show with a *JWST*-selected sample that *HST*-faint sources extend to higher masses than *HST*-dark sources. We therefore move beyond the strict *HST*-dark classification by including *HST*-faint sources in our selection, so as not to miss the most massive and bright galaxies (*HST*-dark classification referenced from Pérez-González et al. 2023). We also use the *F*444*W* band to get the broadest redshift range possible (as the highest redshift sources will have their Balmer break closer to *F*444*W*). Given our choice of using the *F*150*W* and *F*444*W* bands, we identify the *F*150*W*–*F*444*W* colour at which we expect to select galaxies that are (i) high redshift ($z \gtrsim 3$), (ii) massive ($\log M_\star/M_\odot \sim 10$), and (iii) dusty ($A_V \gtrsim 2$ mag). In addition, from the SED-tracks shown in Fig. 1, we estimate the *F*150*W* magnitude at which we rid the sample of low-z sources ($z \lesssim 2$) while retaining the most massive and dusty galaxies in our sample.

Using the SED modelling described above, we determine a selection that is optimized to identify galaxies with $A_V \gtrsim 2$ mag and $\log M_\star/M_\odot \sim 10$ at $z \gtrsim 3$, described in equation (1):

$$\begin{aligned} &F150W - F444W \ > 2.1 \text{ mag}, \\ &F150W > 25 \text{ mag}. \end{aligned} \tag{1}$$

Additionally, as the prominent feature of our galaxies is their redness, this suggests that they must have significant emission in the long wavelength bands. To ensure reliable detections, we require SNR > 5 in all three wide filters in the long wavelength channels: *F*277*W*, *F*356*W*, and *F*444*W*. Altogether, this colour selection is more flexible than in previous studies (i.e. Barrufet et al. 2023); we later remove the $z < 3$ sources after evaluating their physical properties (see Section 4.1).

We find 179 galaxies that satisfy the $F150W - F444W > 2.1$ mag and $F150W > 25$ mag criteria out of the >90 000 sources in our catalogue (see Fig. 1).

2.4 Identifying and removing obscured AGN

In recent literature, there has been mounting evidence from *JWST* of a population of high redshift obscured AGN that displays very red colours in the NIR (Barro et al. 2023; Greene et al. 2023; Matthee et al. 2023; Labbe et al. 2023a). These so-called little red dots (LRDs) have characteristically blue rest-UV colours which possibly arise from star-forming regions, and red rest-optical colours that arise from the hot, dusty torus of the AGN (Greene et al. 2023; Labbe et al. 2023a). These sources are potential contaminants in selections of red, star-forming galaxies, and it is important to address their presence in our sample.

Based on the colour and compactness criteria outlined in Labbe et al. (2023a) and Greene et al. (2023), we identify a parent sample of 29 potential AGN candidates. In order to further identify point-like sources, we perform a two-component PSF + Sérsic fit in the *F*444*W* filter using the GALFITM[4] (Häußler et al. 2013; Vika et al. 2015) software, identifying sources where the flux associated with the PSF component exceeds the flux associated with the Sérsic component (Labbe et al. 2023a). We identify 20 sources that satisfy these criteria.

We remove these 20 sources from our sample during analysis (Section 4 onwards), thus considering a purely star-forming sample of galaxies. Fig. A1 in Appendix A shows the postage stamps and SED of source 6583, identified as one of the 20 AGN candidates in

[3] https://bagpipes.readthedocs.io/en/latest/

[4] https://www.nottingham.ac.uk/astronomy/megamorph/

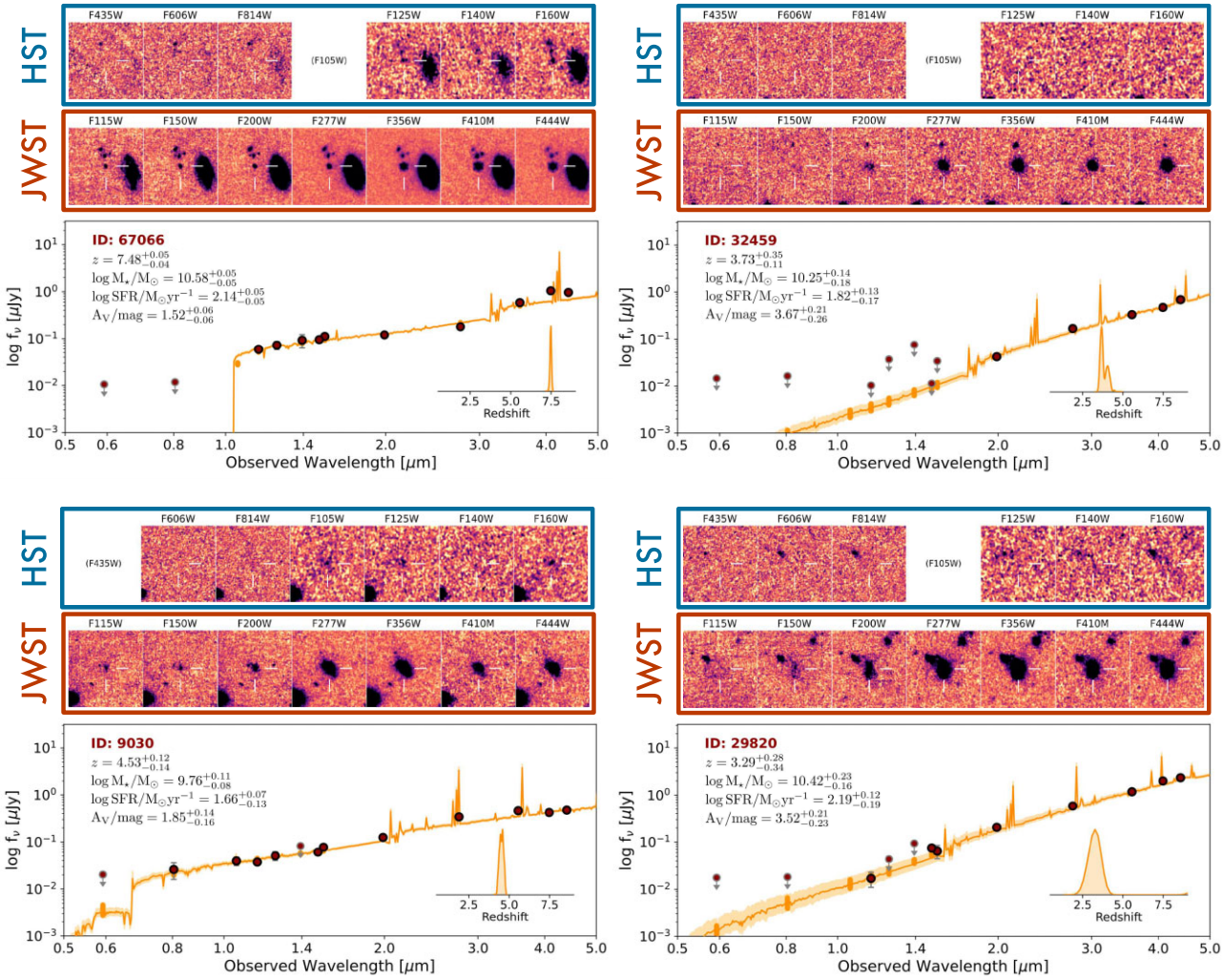

Figure 2. Postage stamps and SED fits of four selected galaxies from our sample of red galaxies. The stamps boxed in blue are from ancillary *HST*/ACS and WFC3 data, and the stamps boxed in red are from *JWST*/NIRCam imaging (each stamp is 4×4 arcsec^2). There is a variety in the morphological properties of our sample, ranging from spatially extended sources to compact ones. The lower panels display the SED fits: the maroon points represent the photometry and the downward arrows represent the flux upper limits. The orange lines are the SED fits from BAGPIPES and the photometric redshift probability density functions are inlaid in the lower right part of the graphs. The physical properties of these galaxies are quoted on the graphs. They are massive ($\log M_\star/M_\odot \gtrsim 9.5$) and dusty ($A_V \sim 1.5 - 4$ mag) with redshifts ranging from $z \sim 3$–8.

our sample selection. Fig. A2 shows the effect of AGN on the SMF, showing that in particular the SMF at $6 < z < 8$ is significantly overestimated by including AGN.

3 SED FITTING WITH BAGPIPES TO DETERMINE THE PHYSICAL PROPERTIES OF GALAXIES

To calculate the physical properties of our sample, we use the PYTHON tool BAGPIPES (Carnall et al. 2018). BAGPIPES is an SED-fitting tool capable of modelling galaxies with various star formation histories (such as delayed-τ, exponential, constant, bursts, etc.) and dust models (Cardelli, Clayton & Mathis 1989; Calzetti et al. 2000; Charlot & Fall 2000, etc.), using stellar population synthesis (SPS) models (Bruzual & Charlot 2003). We choose to use a delayed-τ SFH, which has been shown as an effective SFH to model the bulk of the stellar population, and accurately recover stellar masses (Ciesla, Elbaz & Fensch 2017). Furthermore, this SFH has been successfully used in previous studies of *HST*-dark galaxies and massive galaxies (Wang et al. 2016; Alcalde Pampliega et al. 2019; Wang et al. 2019; Barrufet et al. 2023; Pérez-González et al. 2023).

We perform SED-fitting within a broad parameter space, allowing the code to explore the following ranges: redshifts between $z = (0, 10)$, a delayed-τ SF history with $\tau = (0.1, 9)$ Gyr, masses in the range $\log M_\star/M_\odot = (6, 13)$, metallicities between $Z = (0.2, 1.2)\, Z_\odot$, a Calzetti dust model with $A_V = (0.2, 4)$ mag, nebular emission with an ionization parameter of $\log U = -2$, and a velocity dispersion of 300. The models chosen have been successfully used for similar types of galaxies, being able to fit red SEDs (Wang et al. 2016, 2019; Barrufet et al. 2023). The broad parameter space in each model allows us to explore this enigmatic galaxy population and unveil their physical properties in more detail, in particular their stellar masses.

To test the suitability of our chosen A_V range, we allow A_V to vary from (0, 6) mag, finding that some galaxies are fit to very dusty ($A_V > 4$ mag) solutions at low redshifts ($z < 0.75$). Galaxies with similar properties have been reported in Caputi et al. (2012) and more recently in Bisigello et al. (2023), where BAGPIPES is used. We

compare the redshifts from BAGPIPES with redshifts derived from the Easy and Accurate Zphot from Yale (EAZY) software (Brammer, van Dokkum & Coppi 2008), using the `blue_sfhz` template set.[5] We find that the photo-z's of the $A_V > 4$ mag sources are not in good agreement with EAZY, where EAZY typically finds higher z solutions with lower A_V. This is expected, as the maximum A_V that EAZY can describe is redshift dependent, reaching a maximum of $A_V \sim 4$ at $z \sim 3$. In addition, upon visual inspection of the postage stamps, we find that several of these sources are very compact, completely dropping out of the shorter wavelength filters and thus being more likely to lie at higher redshifts than at $z < 0.75$. The inclusion of MIRI data could potentially rule out the low-z solutions. However, this is only available over a very small portion of the field currently. We refer to Alcalde Pampliega et al. (in preparation) for a more detailed analysis including MIRI data.

Additionally, given that our aim is to derive accurate stellar masses in order to calculate the SMF, we test whether the derived stellar masses change significantly if we use the EAZY photometric redshifts as an input to the BAGPIPES SED fitting. We find that with EAZY-z as an input, $\langle \log M_\star/\mathrm{M}_\odot \rangle = 10.18^{+0.40}_{-0.50}$ and with the BAGPIPES-z, $\langle \log M_\star/\mathrm{M}_\odot \rangle = 10.15^{+0.43}_{-0.50}$. Both derived stellar masses follow a tight 1:1 relation with an average scatter of 0.2 dex, suggesting that the final SMFs will not be strongly affected by our choice of input redshift. We finally use the BAGPIPES-z in all SED fitting.

Examples of some SED fits are shown in Fig. 2, which showcases the variety in galaxy morphology and physical properties. Most of our sources have very red slopes indicating high dust attenuation. We find a diversity in morphology: some sources are spatially extended, while others are extremely compact (see Fig. 2).

We performed a visual inspection of SEDs and postage stamps for all sources while considering their derived physical properties. We remove 11 sources from our sample due to either clearly overestimated photometric redshifts and masses (spatially extended sources that are likely at lower redshift) or sources with deblending issues. Our final sample thus contains 148 galaxies.

To recapitulate, out of the colour-selected sample of 179 galaxies outlined in Section 2.3, we remove 20 AGN candidates (described in Section 2.4) and further remove 11 sources that have poor SED fits, resulting in a final sample of 148 galaxies.

4 PHYSICAL PROPERTIES OF RED, OPTICALLY FAINT GALAXIES

JWST's outstanding sensitivity and resolution in the near-IR allow us to determine photometric redshifts and physical parameters (such as stellar masses, SFRs, etc.) with unprecedented accuracy. This allows us to place tighter constraints on the stellar mass build-up in the early Universe. In this section, we present the photometric redshifts and physical characteristics of our galaxies as determined with BAGPIPES (see Table B1 for a list of the derived physical parameters of our full sample; AGN candidates are denoted as such but removed from the following analysis).

4.1 Photometric redshifts

We determine photometric redshifts for our sample of red galaxies using BAGPIPES (see Section 3). The redshift distribution is shown in Fig. 3. ∼60% of the sample lies at $z \gtrsim 3$ and ∼ 90% at $z \gtrsim 2$, with an average redshift of $z_{\mathrm{mean}} = 3.46$. This shows that our colour selection successfully identifies high redshifts galaxies, out to $z \sim 8$. The redshift is mostly in agreement with EAZY redshifts using standard templates.

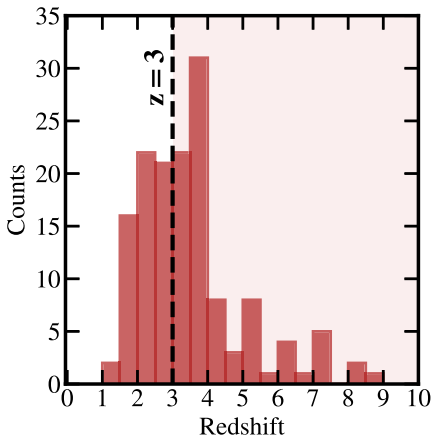

Figure 3. Photometric redshift distribution for 148 red galaxies, determined with the SED-fitting tool BAGPIPES. The average redshift is $z_{\mathrm{mean}} = 3.46$, with the 16th, 50th, and 84th percentiles being 2.11, 3.13, and 4.65. ∼60% of the sample lies at $z > 3$, reaching $z \sim 8$.

We note the significant number of galaxies that lie at $z < 3$ in our selection. We draw the reader's attention back to Fig. 1, where we show with the use of arrows that masses and redshifts increase in opposing directions in the colour space of our selection. Further, at a given redshift and stellar mass, there is a scatter in stellar ages and dust which means that invariably, there is a scatter in the properties of the selected population. Therefore, in order to build the most inclusive sample and so as not to miss the most massive and dusty galaxies, it is unavoidable for low-redshift galaxies to enter our selection.

Further, we draw the reader's attention to a caveat of this selection technique, namely the two local peaks seen in the redshift distribution at $z \sim 5.5$ and $z \sim 7.5$ in Fig. 3. The F444W detection is likely driven by the H α + [N II] lines at $z \sim 4.9$–6.6, and the [O III] + H β lines at $z = 6.9$–9.0 (see Oesch et al. 2023). The samples at these redshifts are thus qualitatively different from the bulk sample because their 'redness' comes from emission lines rather than the continuum. However, we note that our selection includes 5σ detection masks in the long-wavelength filters (*F277W*, *F356W*, and *F444W*), thus ensuring that the continuum is relatively bright over an extended wavelength range and not just in *F444W*. Additionally, as elaborated in the following section, all sources in this study have high A_V magnitudes; therefore, even if the *F444W* fluxes of a few select sources are slightly boosted by emission lines, they still qualify as targets for our study. Furthermore, the red and optically faint selection criteria imply that such sources were missing from previous estimates, further justifying their inclusion in our sample.

4.2 Physical properties of red galaxies

One of *JWST*'s most important improvements in the NIR is its increased photometric coverage at 1–5 μm in comparison with its predecessor, *Spitzer*. This allows *JWST* to better probe the Balmer break and thus derive more accurate photometric redshifts than previously possible. With more accurate photometric redshifts, through SED-fitting we can additionally derive more reliable estimates of the stellar masses of galaxies and their star formation rates.

[5] https://github.com/gbrammer/eazy-photoz/tree/master/templates/sfhz

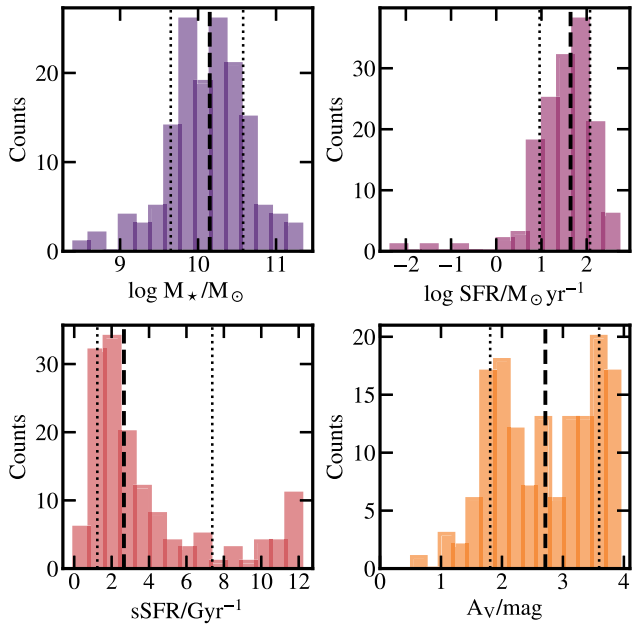

Figure 4. Top left to bottom right: Histograms of stellar masses, SFRs, specific SFRs, and dust attenuations of our sample of 148 red galaxies. The dashed line indicates the 50th percentile, while the dotted lines indicate the 16th and 84th percentiles. Our sample is massive ($\langle \log M_\star/\mathrm{M}_\odot \rangle = 10.15^{+0.43}_{-0.50}$) and dusty ($\langle A_\mathrm{V} \rangle = 2.71^{+0.88}_{-0.91}$ mag), with moderate SFRs of $\langle \log \mathrm{SFR}/\mathrm{M}_\odot\,\mathrm{yr}^{-1} \rangle = 1.64^{+0.43}_{-0.68}$, on average below 50 [$\mathrm{M}_\odot\,\mathrm{yr}^{-1}$] and specific SFRs of $\langle \mathrm{sSFR}/\mathrm{Gyr}^{-1} \rangle = 2.66^{+4.72}_{-1.42}$.

We present the distributions of the physical properties of our sample of 148 red, optically faint galaxies in Fig. 4. We find these galaxies to be massive, with a median stellar mass of $\langle \log M_\star/\mathrm{M}_\odot \rangle = 10.15^{+0.43}_{-0.50}$. They also have high dust attenuations of $\langle A_\mathrm{V} \rangle = 2.71^{+0.88}_{-0.91}$ mag. Additionally, they have moderate star formation rates, with $\langle \log \mathrm{SFR}/\mathrm{M}_\odot\,\mathrm{yr}^{-1} \rangle = 1.64^{+0.43}_{-0.68}$ and $\langle \mathrm{sSFR}/\mathrm{Gyr}^{-1} \rangle = 2.66^{+4.72}_{-1.42}$. As expected, we find our sample to be dominated by relatively massive and dusty star-forming systems.

We note that the SFRs derived in our study are based on rest-frame UV to optical SED fits. We are therefore not modelling the starlight that is reprocessed by dust and emitted in the FIR. While for a more complete picture of the SFR, more FIR data are needed to recover the full IR SED (see e.g. Xiao et al. 2023a), we refer the reader to Williams et al. (2023), where they show with a selection of optically dark galaxies that only those with the most extreme SFRs are significantly affected by the inclusion of MIR and FIR data.

To further illustrate the dusty nature of our galaxies we situate them on the widely used UVJ diagram. We classify the star-forming versus quiescent regions on the UVJ diagram following Williams et al. (2009), and further split the star-forming region into dusty and unobscured zones following the classification in Spitler et al. (2014). Fig. 5 shows the UVJ classification of our galaxies and of the full CEERS sample. Rest-frame colours for our red galaxies are determined by the best-fitting SEDs from BAGPIPES, while for the full CEERS sample they are determined with EAZY due to less expensive computational time. Except for one galaxy lying in the quiescent region of the diagram, the sample lies in the star-forming region, with $\sim 75\%$ of the sample lying particularly in the dusty region. Thus, the UVJ classification further indicates the dust-obscured nature of our sample.

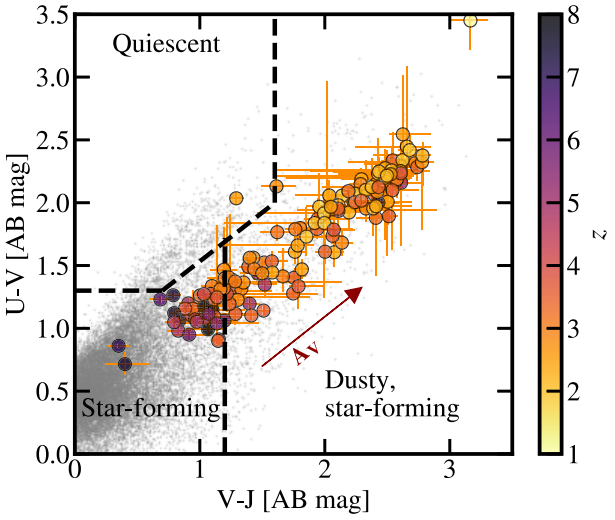

Figure 5. $U-V$ versus $V-J$ colours of our sample (coloured by redshift), and the CEERS sample (grey scatter points). Uncertainties are given by the 16th and 84th percentiles of the posterior distribution from SED-fitting with BAGPIPES. The galaxy classifications indicated by the black dashed lines are adopted from Williams et al. (2009) and Spitler et al. (2014). The red arrow is the reddening vector, indicating the direction in which the dust attenuation increases. All our galaxies (except one) lie in the star-forming regions of the diagram, with $\sim 75\%$ of the sample lying in the dusty star-forming region. There is a clear tendency for less dusty sources to be at higher redshift.

4.3 Red galaxies on the galaxy MS

To place our galaxies within the context of galaxy evolution, we explore their position on the galaxy MS. Fig. 6 shows a plot of SFR versus $M_\star$ for our sample, comparing them to the star-forming MS of galaxies at $z=$ 2, 4, and 6 (from Speagle et al. 2014). As shown, our galaxies lie on the star-forming MS, indicative of the 'normal' nature of their ongoing star formation. The three galaxies lying significantly below the star-forming MS are candidate quiescent galaxies at $z < 3$. They form less than 2% of our sample.

We compare our galaxy sample at $3 < z < 5$ to two studies of interest from the literature: Wang et al. (2019) studied ALMA-detected *HST*-dark galaxies using *HST* and *Spitzer*, and the more recent Barrufet et al. (2023) studied *HST*-dark galaxies with *HST* and *JWST*. The comparison between samples is shown in Fig. 7.

The high-mass end of our sample overlaps with the Wang et al. (2019) sample as our colour selection is inclusive of the Wang et al. (2019) selection criteria. Additionally, the *Spitzer*/IRAC sensitivity is considerably lower than that of *JWST*/NIRCam in the same range, thus resulting in the detection of only the brightest and most massive galaxies. We also select lower-mass galaxies than Wang et al. (2019) as *JWST* can detect galaxies that are fainter in *F*444*W*, and our colour selection is less extreme than that used in Wang et al. (2019).

The low-mass end of our sample overlaps with the range covered by *HST*-dark galaxies from Barrufet et al. (2023). This study specifically looked at *HST*-dark galaxies (F160W > 27 mag), with *JWST*/NIRCam's sensitivity permitting detections of lower mass systems. However, this magnitude cut also limits the detection of brighter, higher mass sources. By using a less restrictive magnitude cut at 1.5 μm ($F150W > 25$ mag) our selection criteria ensure we find higher mass galaxies than in Barrufet et al. (2023) while still including the lower mass *HST*-dark galaxies in their study. In Fig. 7, we show that our sample of red, optically faint

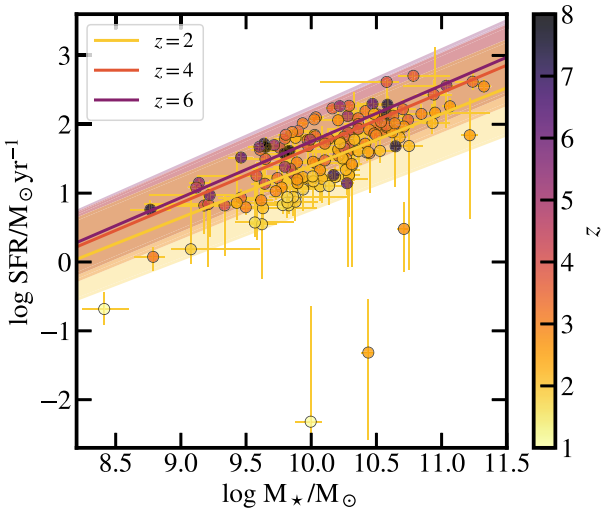

Figure 6. SFR versus stellar mass for our sample of red, optically faint galaxies, coloured by photo-z (circular scatter points). Uncertainties are given by the 16th and 84th percentile of the posterior distribution from SED-fitting with BAGPIPES. The galaxy MS lines shown at $z = 2$, 4, and 6 are from Speagle et al. (2014) (solid coloured lines with scatter). The majority of our sample lies on the MS at redshifts of $z < 6$, suggesting that they are normal star-forming galaxies with moderate SFRs. The three sources lying significantly below the MS are candidate quiescent galaxies.

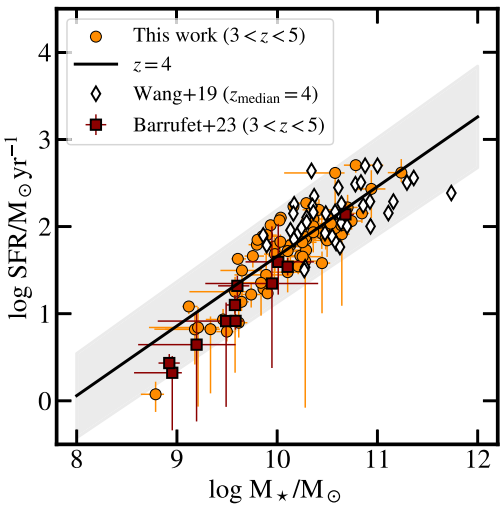

Figure 7. SFR versus stellar mass for the subset of our sample of red, optically faint galaxies at $3 < z < 5$ (circular scatter points). We show the galaxy MS at $z = 4$. from Speagle et al. (2014) (solid line with scatter). We compare our sample to *HST*-dark galaxies from Wang et al. (2019) with $z_{\rm median} = 4$ (empty diamonds), and a sample subset from Barrufet et al. (2023) at $3 < z < 5$ (red squares). Our sample overlaps with the Barrufet et al. (2023) sample at the lower mass end and with the Wang et al. (2019) sample at the high-mass end, showing that our study covers the mass-range spanned by *HST*-dark/faint galaxies in both the pre-*JWST* and *JWST* era.

sources lie on the galaxy MS, similar to *HST*-dark galaxies (Barrufet et al. 2023). The comparison with these select studies from the literature shows that the mass-range spanned by our sample overlaps with both pre-*JWST* and *JWST*-selected *HST*-dark/faint galaxies.

5 STELLAR MASS FUNCTIONS OF RED GALAXIES: FINDING THE MISSING SOURCES THAT DOMINATE THE HIGH-MASS END

In this section, we present the SMFs of red, optically faint galaxies at redshifts of $3 < z < 8$. We describe the method used to derive the SMFs and their uncertainties. The SMFs are then presented, discussed, and compared to studies in the literature.

We note that the sample statistics quoted in the previous section were for the full sample of 148 red galaxies across the whole redshift range shown in Fig. 3. For the 86 galaxies in the redshift range $3 < z < 8$, the average stellar masses and dust attenuation values are $\langle \log M_\star/{\rm M}_\odot \rangle = 10.17^{+0.41}_{-0.56}$ and $\langle A_{\rm V} \rangle = 2.30^{+1.22}_{-0.56}$ mag, setting the stage for the exploration of the SMFs of massive, dust-obscured galaxies at these epochs.

5.1 Determining SMFs

We use the step-wise method to calculate the SMFs of our sample (Bouwens et al. 2008; Santini et al. 2021). The SMFs are approximated by binning the mass distribution, calculating the number of galaxies within each mass bin and dividing this number by the differential comoving volume of the survey. The mass resolution is judiciously chosen to have reasonable statistics within individual mass bins and to have an appropriate mass resolution in order to determine the shape of the SMF.

Given that we detect sources on a stacked image of $F277W + F356W + F444W$ and additionally select sources based on their $F150W$–$F444W$ colour, we determine the area overlapped by all four filters in the CEERS survey, which is 83.3 arcmin^2. We accordingly calculate the differential comoving volume within the considered redshift bins, respectively.

The final SMFs are calculated as shown in equation (2), where $\Phi_{i,j}$ is the estimated number density in a redshift bin 'i' and mass bin 'j' per fixed mass bin $\Delta \log M$. N_j is the number of galaxies in the jth mass bin, ${\rm d}V_{\rm i,\,comoving}$ is the differential comoving volume determined within the ith redshift bin and $f_\star$ is a multiplicative factor derived from a completeness simulation used to account for missing sources in our detection catalogues (described in Section 5.1.1):

$$\Phi_{i,j} = N_j \,/\, ({\rm d}V_{i,\rm comoving} \Delta \log M f_\star). \quad (2)$$

5.1.1 *Completeness*

We measure the source detection completeness by running a simple simulation using our custom version of the publicly available software GLACIAR2 (Carrasco et al. 2018; Leethochawalit et al. 2022). We first select a representative 1.5 arcmin × 1.5 arcmin cut-out approximately in the middle of the CEERS image with average depth and no contamination by bright stars. Using GLACIAR2, we inject artificial sources, spanning a range of input UV magnitudes from -24.4 to -16.2 in 35 bins at a fixed redshift of $z = 6$ into the cut-out. We inject 500 sources per bin in batches of maximally 100 sources at a time to avoid overcrowding and run SOURCEEXTRACTOR with the same settings as outlined in Section 2.2. The injected galaxies follow a Gaussian distribution in the logarithm of the effective radius, centred at 0.8 kpc and with a scatter of 0.17 dex and they have Sérsic light profiles with 50% of the galaxies having a Sérsic index of 1.5, and 25% having indices of 1 and 2, respectively. We further assume a flat SED (i.e. a fixed UV slope of $\beta = -2$), since we only wish to estimate the completeness as a function of apparent magnitude. We repeat this experiment 10 times, therefore injecting 175 000 sources in total.

To obtain the completeness of our sample, we first measure the fraction of recovered galaxies as a function of the input magnitude. Then, for each bin in apparent output magnitude, we determine the completeness as the weighted mean of the completeness values found in each input magnitude bin, weighted by the number of sources from that bin that were observed in the given output magnitude bin. Then, we additionally determine the fraction of detected sources in each apparent magnitude bin that have a measured SNR > 5 in all of *F277W*, *F356W*, and *F444W* (cf. Section 2.3) and multiply that fraction with the detection completeness obtained in the previous step. Since all the observed galaxies considered in this paper have AB-magnitudes $\lesssim 27$ in *F444W*, they are in a regime where the completeness is high and approximately constant as a function of the apparent magnitude (e.g. in *F444W*). From our analysis, we derive a mean completeness factor of $f_\star = 0.87$ by which we scale all our mass functions (see equation 2).

To determine the mass limit above which we are 80% mass complete, we project our mass distribution onto the SNR limit of our selection (see e.g. Pozzetti et al. 2010). Given that we select sources that are detected with a 5σ certainty in *F444W*, *F356W*, and *F277W*, the SNR limit of our selection is $\mathrm{SNR_{lim}} = 5\sqrt{3}$. We calculate the joint SNR for all sources in our sample as $\mathrm{SNR^2_{joint}} = \mathrm{SNR^2_{F277W}} + \mathrm{SNR^2_{F356W}} + \mathrm{SNR^2_{F444W}}$. Assuming that stellar mass values linearly scale with source brightness, we find the hypothetical mass that each source would have if detected at $\mathrm{SNR_{lim}}$: $\log M_{\mathrm{hypothetical}} = \log M_\star - \log(\mathrm{SNR_{joint}}/\mathrm{SNR_{lim}})$. The 80th percentile of the $M_{\mathrm{hypothetical}}$ distribution provides the limit above which the sample is 80% mass complete, given the specific mass-to-light ratios and SEDs in our sample. We determine that the 80% mass complete limits are $\log M_\star/\mathrm{M}_\odot = 9.15$ at $3 < z < 4$, $\log M_\star/\mathrm{M}_\odot = 9.07$ at $4 < z < 6$ and $\log M_\star/\mathrm{M}_\odot = 9.21$ at $6 < z < 8$. Therefore, in general, we find that our sample is 80% mass complete above $M_\star/\mathrm{M}_\odot \sim 9.25$ in all redshift bins, and therefore we plot SMFs above this conservative limit. We lose a negligible number of sources by limiting the sample in this manner (one source each in the redshift bins $3 < z < 4$ and $6 < z < 8$).

To consider the completeness of our sample given the flux density limits of the telescope survey, we consider the widely used V/V_{max} correction, used to test uniformity in the spatial distribution of sources [Schmidt (1968), see also Weaver et al. (2023b) for a detailed discussion] that particularly affects faint sources. This method considers the maximum redshift, z_{max}, at which a source within a bin $z_{\mathrm{low}} < z < z_{\mathrm{high}}$ would still be observable before falling below the detection limit. Each source is then associated with a maximum observable differential comoving volume, V_{max}, associated with z_{max}, and the actual differential comoving volume it is detected in, V, associated with z_{high}. If $z_{\mathrm{max}} < z_{\mathrm{high}}$, the source is given a weight of V/V_{max}, and if $z_{\mathrm{max}} > z_{\mathrm{high}}$, $V/V_{\mathrm{max}} = 1$ (as the source would anyways have been detected in the survey, and therefore does not need to be given a higher weightage). Like the step-wise method used to calculate the SMF, the V/V_{max} too is non-parametric. It assumes no functional form for the SMF, but it does assume a uniform spatial distribution of galaxies. However, Weaver et al. (2023b) show that this is problematic only at $z < 1$, thus not affecting our study. We apply the V/V_{max} correction to our sources, finding that given the redshift bins we choose, no galaxies in our sample require this correction. This is expected, as our galaxies are red by definition and on average massive and therefore bright in *F444W*. The V/V_{max} correction mostly affects only faint galaxies with the propensity to be detected close to the noise threshold.

5.1.2 *Sources of uncertainty*

We estimate the uncertainty of the SMFs by considering the Poisson noise, σ_{N}, the uncertainty due to cosmic variance, σ_{cv}, and the systematic uncertainty, σ_{sys}, due to SED-fitting.

Given that the calculation of the SMF is fundamentally a discrete counting process, the distribution of galaxies within a particular redshift and mass bin must follow Poissonian statistics. We calculate the uncertainty, σ_{N}, by using frequentist central confidence intervals[6] (for details, see Maxwell 2011).

An added factor of uncertainty arises from cosmic variance, the field-to-field variation in galaxy number counts due to large-scale structure. It becomes an important source of uncertainty in narrow and deep surveys (Somerville et al. 2004), and is routinely included in uncertainty estimates of the SMF (Davidzon et al. 2017; McLeod et al. 2021; Weaver et al. 2023b). To estimate the cosmic variance, σ_{cv}, we use the CosmicVarianceCalculator v1.03[7] (Trenti & Stiavelli 2008), evaluated at the respective number density of our sample. We find relative cosmic variances for our sample to lie between 20% and 30%, with the cosmic variance increasing with stellar mass.

Uncertainties on redshifts and stellar masses can give rise to a scatter, σ_{fit}, due to SED fitting. In order to estimate σ_{fit}, we generate 1000 independent realizations of the SMF by sampling from the posterior distributions of physical properties derived with BAGPIPES and calculate the variance of the number densities from these realizations. This method provides an estimate of the SMF as well as the uncertainty, σ_{fit}, on the SMF.

The final uncertainty, σ_{tot}, of the SMF is the quadrature addition of the Poisson uncertainty, cosmic variance, and the uncertainty due to SED fitting (as done in Davidzon et al. 2017), calculated via equation (3):

$$\sigma^2_{\mathrm{tot}} = \sigma^2_{\mathrm{N}} + \sigma^2_{\mathrm{cv}} + \sigma^2_{\mathrm{fit}}. \tag{3}$$

In the absence of detections, upper limits are calculated as the right confidence interval of the Poisson distribution. This is $1.841/(\mathrm{d}V_{i,\mathrm{comoving}}\,\Delta \log M)$ following Gehrels (1986).

5.2 SMFs at $3 < z < 8$

Fig. 8 and Tables 2 and 3 present the SMFs of our sample in three redshift ranges: $3 < z < 4$, $4 < z < 6$, and $6 < z < 8$, calculated using the method outlined in the previous section. We compare our dust obscured SMFs to the observed pre-*JWST* total SMFs from Weaver et al. (2023b), McLeod et al. (2021), and Stefanon et al. (2021), derived from ground- and space-based observations. We also compare our SMFs to model dust-obscured SMFs from Long et al. (2023b), which are derived from semi-empirical simulations of DSFGs.

In order to determine the previously *missed* fraction of the SMF, we assume that together, the selection functions of our study and pre-*JWST* studies produce a more complete survey than solely pre-*JWST* studies. Therefore, we compute upper limits on the previously missed fraction of the SMF by dividing our SMF by the sum of our SMF with the pre-*JWST* SMF from Weaver et al. (2023b).

The left-hand panel of Fig. 8 shows our SMF at $3 < z < 4$ in comparison with Weaver et al. (2023b) (at $z \sim 3.0$–3.5) and McLeod et al. (2021) (at $z \sim 3.25$). At all masses shown in this redshift range, the SMF of our sample lies below the pre-*JWST* SMF from Weaver

[6] https://docs.astropy.org/en/stable/api/astropy.stats.poisson_conf_interval.html

[7] https://www.ph.unimelb.edu.au/~mtrenti/cvc/CosmicVariance.html

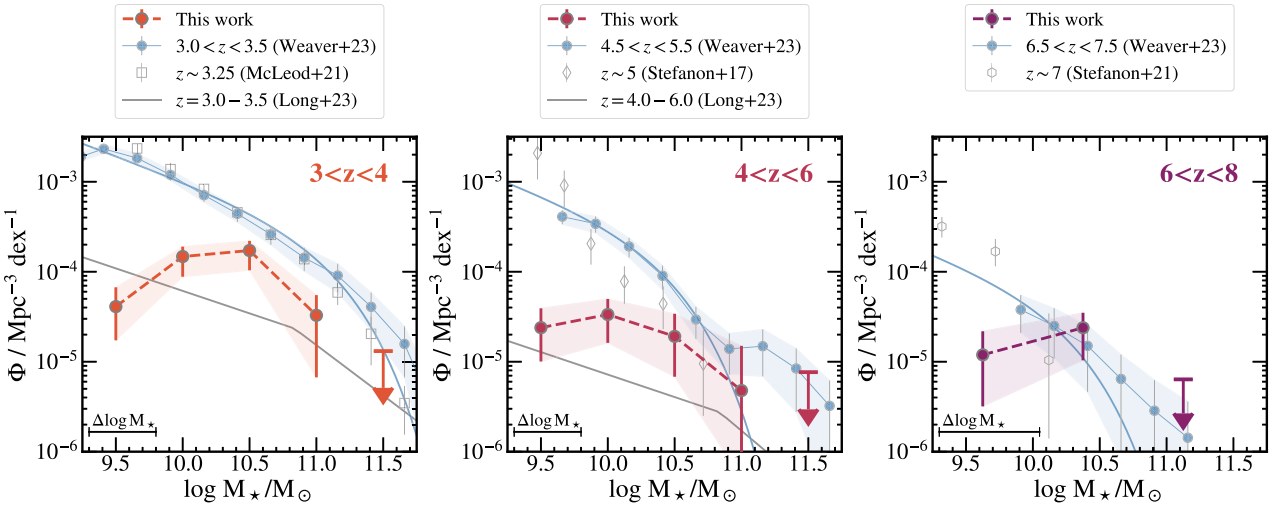

Figure 8. SMFs of our sample of massive and dusty galaxies in three redshift ranges: $3 < z < 4$, $4 < z < 6$, and $6 < z < 8$. Uncertainties shown are derived from Poisson statistics, cosmic variance, and scatter due to SED fitting. Upper bounds (downward arrows) are derived from the right confidence interval of the Poisson distribution. The fixed size of the mass bins are shown in the lower left of each panel. We compare our results to the observed SMFs of the pre-*JWST* total galaxy population from Weaver et al. (2023b) (blue scatter points and shaded area) derived from COSMOS2020 observations (Weaver et al. 2023a) and to the model SMFs from Long et al. (2023b) (solid grey line) derived from semi-empirical simulations for DSFGs. For reference, the Schechter fits from Weaver et al. (2023b) are also shown (solid blue line). The SMF at $3 < z < 4$ is additionally compared to McLeod et al. (2021) (square scatter points), derived from ground-based observations, and the $4 < z < 6$ and $6 < z < 8$ SMFs are compared to Stefanon et al. (2017b) and Stefanon et al. (2021) at $z = 5$ and $z = 7$, respectively (diamond and hexagon scatter points), derived from *HST* and *Spitzer* imaging. At $3 < z < 4$, comparing our SMF to the pre-*JWST* Weaver et al. (2023b) SMF suggests that up to $\sim 30\%$ of the galaxy population could have been missed at $\log M_\star/\mathrm{M}_\odot = 10.5$ and up to $\sim 20\%$ at $\log M_\star/\mathrm{M}_\odot = 11.0$; similarly at $4 < z < 6$, we find missed fractions of up to $\sim 25\%$ at $\log M_\star/\mathrm{M}_\odot = 10.5$ and 11.0. At $6 < z < 8$, the obscured SMF exceeds the pre-*JWST* SMF from Weaver et al. (2023b) at $\log M_\star/\mathrm{M}_\odot = 10.375$. At both $3 < z < 4$ and $4 < z < 6$, our SMFs dominate the dusty model SMF predicted by Long et al. (2023b) at $\log M_\star/\mathrm{M}_\odot > 9.5$.

Table 2. SMF values of massive and dusty galaxies at $3 < z < 4$ and $4 < z < 6$, as shown graphically in the first two panels of Fig. 8. Uncertainties are calculated as the quadrature addition of Poissonian noise, cosmic variance, and scatter due to SED fitting.

$\log M_\star/\mathrm{M}_\odot$	Φ / 10^{-5} Mpc^{-3}dex^{-1}	
	$3 < z < 4$	$4 < z < 6$
9.5	$4.10^{+2.62}_{-2.37}$	$2.39^{+1.53}_{-1.38}$
10.0	$14.74^{+4.26}_{-5.95}$	$3.35^{+1.64}_{-1.73}$
10.5	$17.21^{+4.82}_{-6.83}$	$1.91^{+1.45}_{-1.23}$
11.0	$3.28^{+2.22}_{-2.61}$	$0.48^{+1.02}_{-0.43}$
11.5	<1.31	<0.77

Table 3. SMF values of massive and dusty galaxies at $6 < z < 8$, as shown graphically in the third panel of Fig. 8. Uncertainties are calculated as the quadrature addition of Poissonian noise, cosmic variance, and scatter due to SED fitting.

$\log M_\star/\mathrm{M}_\odot$	Φ / 10^{-5} Mpc^{-3}dex^{-1}
	$6 < z < 8$
9.625	$1.19^{+0.99}_{-0.87}$
10.375	$2.38^{+1.11}_{-1.35}$
11.125	<0.64

et al. (2023b) (based on COSMOS2020 observations; see Weaver et al. 2023a) and McLeod et al. (2021) (based on *HST* and ground-based observations). The $3 < z < 4$ SMF deviates the most at the low-mass end but comes closest to the pre-*JWST* study at the high-mass end, suggesting that up to $\sim 30\%$ of the galaxy population could have been missed in the pre-*JWST* SMF from Weaver et al. (2023b) at $\log M_\star/\mathrm{M}_\odot \sim 10.5$ and up to $\sim 20\%$ could have been missed at $\log M_\star/\mathrm{M}_\odot \sim 11.0$ – dusty galaxies detected with *JWST* therefore make up a sizeable fraction of the galaxy population at the high-mass end, which suggests that galaxies at the high-mass end have been missing from our galaxy census in this epoch. Further, above $\log M_\star/\mathrm{M}_\odot \sim 9.5$, our SMF at $3 < z < 4$ is significantly higher than the model SMF from Long et al. (2023b) (at $z \sim 3.0$–3.5), with the difference being most pronounced at $\log M_\star/\mathrm{M}_\odot \sim 10.5$. Therefore, we could be seeing an emergent population of MS dusty galaxies that are distinct from the widely studied DSFGs, which are typically more strongly star forming [and which the Long et al. (2023b) simulation is based on]. These results indicate that a significant population of obscured galaxies are prevalent at this redshift range.

At $4 < z < 6$ (central panel of Fig. 8), we compare the SMF of our sample to Weaver et al. (2023b) (at $z \sim 4.5$–5.5). For reference, the Stefanon et al. (2017b) mass function for LBGs at $z = 5$ is shown. Of particular interest in this epoch is the comparison of our sample to the pre-*JWST* SMF at the high-mass end, where at $\log M_\star/\mathrm{M}_\odot \sim 10.5$ and 11.0, we find that up to $\sim 25\%$ of the SMF could have been missed in the Weaver et al. (2023b) mass function. In addition, like at $3 < z < 4$, we find an SMF at $4 < z < 6$ which is significantly higher than the dust-obscured model SMF predicted by the Long et al. (2023b) simulation at $z \sim 4.0$–6.0.

At $6 < z < 8$ (the right panel of Fig. 8), we compare our SMF to Weaver et al. (2023b) (at $z \sim 6.5$–7.5). For reference, the Stefanon et al. (2021) mass function at $z = 7$ is shown. Above $\log M_\star/\mathrm{M}_\odot \sim 10.0$, our sample overtakes the Weaver et al. (2023b)

SMF and exceeds it at $\log M_\star/\mathrm{M}_\odot = 10.375$. This suggests the emergence of an extensive population of galaxies in the Epoch of Reionization, hidden in the pre-*JWST* era but constituting a dominant part of the high-mass population.

We see a strong evolution in our SMFs around $z \sim 4$ between masses of $9.5 \lesssim \log M_\star/\mathrm{M}_\odot \lesssim 11.0$. Comparing the SMFs at $4 < z < 6$ and $3 < z < 4$ in Table 2, we see an increase by a factor of ~ 4 at $\log M_\star/\mathrm{M}_\odot \sim 10.0$, ~ 9 at $\log M_\star/\mathrm{M}_\odot \sim 10.5$, and ~ 7 at $\log M_\star/\mathrm{M}_\odot \sim 11.0$ – this shows an accelerated evolution in the knee of the SMF at this epoch, suggesting the onset of rapid dust-obscured stellar mass growth at $z \sim 4$.

The SMFs of our sample between $4 < z < 6$ and $6 < z < 8$ show little evolution. At the high-mass end, we do not see a strong evolution across the whole redshift range, but we are heavily limited by small sample statistics, systematic uncertainties and cosmic variance, making it challenging to comment on SMF properties without a larger sample.

Globally, our analysis of red, dust-obscured galaxies shows that these sources recover a sizeable fraction of the high-mass end of the pre-*JWST* SMFs from Weaver et al. (2023b). Not only does this reveal the nature of the massive galaxy population, it highlights the efficiency of *JWST* in characterising the massive end of the galaxy SMF.

5.3 Integrated stellar mass density

The cosmic stellar mass density (SMD) is an efficient measure of stellar mass assembly. The total SMD is tightly coupled with the cosmic star formation rate history, and thus could provide insights into early galaxy build-up such as previous epochs of star formation and the stellar IMF of early stellar populations (Dickinson et al. 2003). Multiple works have observationally tracked the evolution of the SMD (Stark et al. 2009; González et al. 2010; Davidzon et al. 2017; McLeod et al. 2021; Weaver et al. 2023b), reaching up to $z \sim 8$–10 (e.g. Stefanon et al. 2021; Weaver et al. 2023b). The observationally determined SMD, however, can be substantially affected if a significant population of high-mass galaxies have been missing in previous observations. This work in part aims to determine the fraction by which pre-*JWST* studies have underestimated the SMD.

We integrate the measured SMFs presented in Section 5.2 in order to get an estimate of the SMD for our galaxy sample. For each redshift bin 'i', we numerically integrate over the mass bins indexed by 'j' following equation (4):

$$\rho_i = \sum_{j=M_{\min}}^{M_{\max}} \Phi_{i,j} M_j \Delta \log M, \tag{4}$$

where $\Phi_{i,j}$ is the SMF value inferred via equation (2), M_j is the central mass within each mass bin, $\Delta \log M$ is the fixed mass bin size, and the limits are given by the mass range covered by our SMFs. Uncertainties on ρ_i are calculated via addition in quadrature, where the upper limits in the SMFs contribute to the upper uncertainty on ρ_i.

We find that the SMD in units of $[10^5\ \mathrm{M}_\odot\ \mathrm{Mpc}^{-3}]$ is $51.6^{24.8}_{-17.2}$ at $3 < z < 4$, $7.5^{+13.4}_{-3.0}$ at $4 < z < 6$ and $4.6^{+6.7}_{-2.4}$ at $6 < z < 8$. The large uncertainty estimates reflect the uncertainty in the SMFs where we are limited by sample size, especially at the high-mass end. Additionally, the upper limits in the highest mass bins make sizeable contributions to the upper uncertainties on the SMD.

In order to determine the missed SMD fraction in pre-*JWST* studies at the high-mass end, we compare our results with the Weaver et al. (2023b) study. As similarly explained in Section 5.2, we calculate an upper limit on the missed SMD fraction as the SMD of our sample divided by the sum of our SMD and the Weaver et al. (2023b) observed SMD, based on the assumption that our two studies together form a more complete survey than pre-*JWST* studies alone.

We integrate the observed SMFs from Weaver et al. (2023b) (shown in Fig. 8) in order to estimate the observed pre-*JWST* total SMD. Given that the Weaver et al. (2023b) SMFs do not reach the lower mass limit of our study at $4 < z < 6$ and $6 < z < 8$, we expand the Weaver + 23 SMFs to lower masses with their Schechter fits down to $\log M_\star/\mathrm{M}_\odot = 9.25$, so as to perform a mass-consistent comparison with our sample. We find missed SMD fractions of $19^{+9}_{-6}\%$ at $3 < z < 4$ and $15^{+26}_{-6}\%$ at $4 < z < 6$. At $6 < z < 8$, we find a missed fraction of $46^{+66}_{-24}\%$, possibly doubling the SMD at this epoch. Therefore, our results indicate that the SMD could have been underestimated in pre-*JWST* studies, in particular significantly at $z > 6$. In future studies, it will be imperative to include dust-obscured galaxies at the high-mass end in order to accurately trace stellar mass build-up in the early Universe.

6 DISCUSSION

In this section, we discuss the results of our work in the context of similar studies conducted with *JWST*'s first year of observations on dusty galaxies. We additionally discuss the abundance of massive galaxies that is suggested by our dust-obscured SMFs, compare our SMD estimates with the SMDs estimated from integrating the Weaver et al. (2023b) Schechter functions, discuss the move towards redder selection functions, and place this in the context of past work and future studies on galaxy censuses.

6.1 Comparison of sample to recent literature in CEERS

JWST's pilot year has seen the output of a great amount of science, with several papers and teams already providing novel insights into obscured galaxies at $z > 3$ (e.g. Akins et al. 2023; Barrufet et al. 2023; Nelson et al. 2023; Pérez-González et al. 2023; Rodighiero et al. 2023; Labbé et al. 2023b). Additionally, it was shown that very dusty galaxies can sometimes contaminate extremely high redshift selections (e.g. Naidu et al. 2022; Arrabal Haro et al. 2023; Zavala et al. 2023). Here, we discuss our sample in comparison with some select studies in the CEERS field: Barrufet et al. (2023), Pérez-González et al. (2023), Labbé et al. (2023b), and Naidu et al. (2022).

Barrufet et al. (2023) studied *HST*-dark galaxies in the CEERS field, identifying massive, obscured galaxies at $z > 3$ and into the Epoch of Reionization. Of the 30 *HST*-dark sources in their study, we identify 12 in our sample, likely due to the different colour selection. Our SMF results support the findings of Barrufet et al. (2023) that suggest that a significant fraction of massive, obscured sources were previously missing from our galaxy census at $z > 3$.

Pérez-González et al. (2023) studied *HST*-dark and -faint galaxies in the first four NIRCam pointings of the CEERS field, using a selection based on $F150W$–$F356W$ colours. Out of their sample of 138 *HST*-dark galaxies, we identify 65 sources in our sample. Comparing their total sample to our study, we find similar redshift ranges ($\langle z \rangle = 3.68^{+1.60}_{-1.00}$ in their study, $\langle z \rangle = 3.46^{+2.04}_{-1.35}$ in ours) and stellar masses ($\langle \log M_\star/\mathrm{M}_\odot \rangle = 10.20^{+0.46}_{-0.73}$ in their study, $\langle \log M_\star/\mathrm{M}_\odot \rangle = 10.15^{+0.43}_{-0.50}$ in ours). We note however that our redshift distribution has a longer high-end tail, where we find more sources at $z \gtrsim 6$ than the Pérez-González et al. (2023) study. This is most likely because we use the longer wavelength $F444W$ filter

in our colour selection, where we are possibly picking up the [O III] line at $z \sim 7$.

Using a selection based on blue rest-UV and red rest-optical colours, Labbé et al. (2023b) found six massive galaxies ($M_\star/\mathrm{M}_\odot > 10^{10}$) at $7.4 < z < 9.1$. We identify two of their sources in our sample (IDs 48 444 and 67066). We most likely do not select the remaining four sources in Labbé et al. (2023b) due to their blue rest-UV colour selection. Additionally, one of the Labbé et al. (2023b) sources originally identified as a massive galaxy at $z = 8.13$ has now been spectroscopically determined to be a likely AGN candidate at $z = 5.64$ (Kocevski et al. 2023); we do not find this source in our sample.

Naidu et al. (2022) proposed a luminous candidate $z \approx 17$ or $z \approx 5$ galaxy, dubbed 'Schrodinger's Galaxy', now confirmed to be an obscured source at $z = 4.912 \pm 0.001$ (Arrabal Haro et al. 2023). We find this galaxy in our sample (ID 81918) at $z = 4.79^{+0.05}_{-0.08}$ with a dust attenuation of $A_\mathrm{V} = 1.74^{+0.11}_{-0.17}$ mag. Such studies show that there is increasing evidence for a population of massive, obscured galaxies at high redshifts, close to and into the Epoch of Reionization (see also Fudamoto et al. 2021).

6.2 Abundance of red galaxies at the high-mass end of SMFs

The SMFs of *JWST*-detected dust-obscured galaxies in our study point toward an abundance of galaxies at the massive end of the pre-*JWST* SMF, possibly leading to an excess of the galaxy population with respect to the pre-*JWST* determined SMF. This abundance is even more pronounced with respect to the Schechter fits from Weaver et al. (2023b) (solid lines in Fig. 8). Comparing our SMD estimates to those found by integrating the Schechter fits from Weaver et al. (2023b) down to $\log M_\star/\mathrm{M}_\odot = 9.25$, we find missed SMD fractions of 19^{+9}_{-6}% at $3 < z < 4$ and 18^{+32}_{-7}% at $4 < z < 6$. At $6 < z < 8$, we find a missed SMD fraction of 52^{+76}_{-27}%, effectively doubling the SMD at this epoch. This excess with respect to the Schechter fit at the massive end of the SMFs at $z \sim 3$–5 was shown in Weaver et al. (2023b) with a sample of 2 μm-selected sources from the COSMOS2020 data set, with hints that this population could be star-forming, dusty galaxies.

It is evident from past work that selecting sources deeper into the NIR results in stronger constraints on the high-mass end of SMFs. At its time, the Weaver et al. (2023b) study represented some of the reddest SMFs in comparison with earlier studies (e.g. Davidzon et al. 2017; Stefanon et al. 2017b, 2021). The effect of this is evident from Fig. 8, where the Weaver et al. (2023b) SMF overtakes the LBG-based Stefanon et al. (2017b) SMF at $4 < z < 6$ and the Stefanon et al. (2021) SMF at $6 < z < 8$ at the high-mass end. Now, with *JWST*/NIRCam allowing us to move even deeper into the NIR regime, our study represents the natural next step in the move towards more complete selections: with sources selected based on their 1.5–4.44 μm colour, our study enables a more complete characterization of massive and dusty galaxies than was possible with previous SMF studies.

Our results reinforce the conclusion that dust-obscured galaxies contribute significantly to the high-mass end of the SMF. In future galaxy censuses with JWST, it will be critical to explore how the SMF measurements at the high-mass end compare with the Schechter formalism of our description of galaxy evolution.

7 SUMMARY AND CONCLUSION

In this work, we used data from the JWST/CEERS survey (Finkelstein et al. 2022, 2023) in the CANDELS/EGS field to identify red, optically-faint galaxies at high redshifts in order to determine the obscured SMF at various epochs in the first two billion years of the history of the Universe. Some key results are summarized in the following:

(i) Using a colour criterion designed to select red, optically faint galaxies, we show that we efficiently select massive and dusty galaxies ($\langle \log M_\star/\mathrm{M}_\odot \rangle = 10.15^{+0.43}_{-0.50}$ and $\langle A_\mathrm{V} \rangle = 2.71^{+0.88}_{-0.91}$ mag) with a majority lying at $z > 3$ (see Figs 3 and 4).

(ii) Our sample contains predominantly star-forming galaxies, largely lying on the star-forming MS. They therefore represent a normal population of galaxies without extreme starburst properties (see Figs 5 and 6). Our sample overlaps with the Wang et al. (2019) sample at the high-mass end and the Barrufet et al. (2023) sample at the low-mass end, showing that our sample of red galaxies has similar star-forming properties to that of *HST*-dark galaxies (see Fig. 7).

(iii) Our analysis of the obscured galaxy SMF (see Fig. 8) shows that in the pre-JWST era, we have missed a significant fraction of galaxies, particularly at the high-mass end of the SMF at redshifts of $z > 3$. The SMFs of red, optically faint galaxies suggest a missed fraction of $\gtrsim 20$% of the galaxy population in the $3 < z < 4$ and $4 < z < 6$ epochs (at $\log M_\star/\mathrm{M}_\odot \geq 10.5$). At $6 < z < 8$, our SMF overtakes the pre-*JWST* SMF from Weaver et al. (2023b) around $\log M_\star/\mathrm{M}_\odot \sim 10.375$.

(iv) Our results at $6 < z < 8$ highlight the importance of accounting for massive, dust-obscured galaxies in the final stages of the Epoch of Reionization.

(v) Our SMFs show a strong evolution at $z \sim 4$ at masses of $9.5 \lesssim \log M_\star/\mathrm{M}_\odot \lesssim 11.0$, suggesting the onset of rapid dust-obscured stellar mass assembly in this epoch.

(vi) The derived SMD of our sources at $\log M_\star/\mathrm{M}_\odot \geq 9.25$ suggests that the missed SMD fraction could be a factor of ∼15–20% at $z \sim 3$–6. We find a missed fraction of ∼45% at $z \sim 6$–8, possibly doubling the SMD at this epoch.

These findings point towards an emergent population of massive, obscured galaxies from $z \sim 3$ up to and into the Epoch of Reionization, supporting the findings of early *JWST* studies (e.g. Akins et al. 2023; Barrufet et al. 2023; Labbé et al. 2023b). The strong evolution of the SMF at $z \sim 4$ suggests that this is a period of rapid stellar mass growth in obscured galaxies. Interestingly, $z \sim 4$ is also roughly when the obscured SFRD is thought to overtake the unobscured SFRD, dominating the cosmic star formation history at later epochs (e.g. Bouwens et al. 2020, 2021; Zavala et al. 2021).

Our results indicate that obscured stellar mass assembly occurred as early as $z \sim 8$, suggesting that the build-up of dusty galaxies could begin close to 600 Myr after the big bang. To further explore the beginning of obscured stellar mass assembly and push the observable redshift boundary farther back, studying the SMF by collating all public *JWST* surveys is critical. Including surveys such as COSMOS-Web (GO-1727, PI: Casey; Casey et al. 2023), PRIMER (GO-1837, PI: Dunlop), UNCOVER (GO-2561, PI: Labbe; Bezanson et al. 2022), and PANORAMIC (GO-2514, PI: Williams) will satisfy the need of the hour: larger sample sizes. These surveys, and others to come with *JWST*, will surely result in us establishing a complete census of the massive, dust-obscured galaxy population in the early Universe.

ACKNOWLEDGEMENTS

The work presented in this paper is based on observations made with the NASA/ESA/CSA *JWST*. The data were obtained from the Mikulski Archive for Space Telescopes at the Space Telescope Sci-

ence Institute, which is operated by the Association of Universities for Research in Astronomy, Inc., under NASA contract NAS 5–03127 for *JWST*. These observations are associated with program #1345.

This work has received funding from the Swiss State Secretariat for Education, Research and Innovation (SERI) under contract number MB22.00072, as well as from the Swiss National Science Foundation (SNSF) through project grant 200020_207349. The Cosmic Dawn Center (DAWN) is funded by the Danish National Research Foundation under grant no. 140.

We thank the anonymous reviewer for their constructive feedback and close reading of the manuscript which helped improve the clarity of this paper. We thank Rui Marques-Chaves, Ivan Kramarenko and Damien Korber for useful discussions that helped improve the quality of this work. RG gratefully acknowledges support from the Inlaks Shivdasani Foundation. YF acknowledges support from NAOJ ALMA Scientific Research grant number 2020–16B and support by JSPS KAKENHI grant number JP23K13149. VG gratefully acknowledges support by the ANID BASAL project FB210003 and from ANID FONDECYT Regular 1221310. For RPN, support for this work was provided by NASA through the NASA Hubble Fellowship grant no. HST-HF2-51515.001-A awarded by the Space Telescope Science Institute, which is operated by the Association of Universities for Research in Astronomy, Incorporated, under NASA contract NAS5-26555. MS acknowledges support from the CIDEGENT/2021/059 grant, from project PID2019-109592GB-I00/AEI/10.13039/501100011033 from the Spanish Ministerio de Ciencia e Innovación – Agencia Estatal de Investigación. MS also acknowledges the financial support from the MCIN with funding from the European Union NextGenerationEU and Generalitat Valenciana in the call Programa de Planes Complementarios de I+D + i (PRTR 2022) Project (VAL-JPAS), reference ASFAE/2022/025. The work of CCW is supported by NOIRLab, which is managed by the Association of Universities for Research in Astronomy (AURA) under a cooperative agreement with the National Science Foundation.

Telescope facilities: *JWST* (NIRCam), *HST* (ACS and WFC3)

Several publicly available softwares have facilitated this work. We extend our thanks to the authors of the following softwares: IPYTHON (Perez & Granger 2007), JUPYTER (Kluyver et al. 2016), ASTROPY (Astropy Collaboration et al. 2013, 2018), MATPLOTLIB (Hunter 2007), NUMPY (Oliphant 2015), PHOTUTILS (Bradley et al. 2022), SCIPY (Virtanen et al. 2020), EAZY (Brammer et al. 2008), BAGPIPES (Carnall et al. 2018), GALFITM (Häußler et al. 2013; Vika et al. 2015), GRIZLI (Brammer 2018), SEXTRACTOR (Bertin & Arnouts 1996), PYPHER (Boucaud et al. 2016), EXTINCTION (Fitzpatrick & Massa 2007), GLACIAR2 (Carrasco et al. 2018; Leethochawalit et al. 2022).

DATA AVAILABILITY

The *JWST* and *HST* raw data products used in this work are available via the Mikulski Archive for Space Telescopes (https://mast.stsci.edu). The combined mosaics are available on github (https://github.com/gbrammer/grizli/blob/master/docs/grizli/image-release-v6.rst). Additional data presented in this work will be made available by the authors upon request.

REFERENCES

Akins H. B. et al., 2023, ApJ, 956, 61
Alcalde Pampliega B. et al., 2019, ApJ, 876, 135
Anderson J., King I. R., 2000, PASP, 112, 1360
Arrabal Haro P. et al., 2023, Nature, 622, 707
Astropy Collaboration et al., 2013, A&A, 558, A33
Astropy Collaboration et al., 2018, AJ, 156, 123
Barro G. et al., 2024, ApJ 963 128
Barrufet L. et al., 2023, MNRAS, 522, 449
Bertin E., Arnouts S., 1996, A&AS, 117, 393
Bezanson R. et al., 2022, preprint (arXiv:2212.04026)
Bisigello L. et al., 2023, A&A, 676, A76
Boucaud A., Bocchio M., Abergel A., Orieux F., Dole H., Hadj-Youcef M. A., 2016, A&A, 596, A63
Bouwens R. et al., 2020, ApJ, 902, 112
Bouwens R. J. et al., 2021, AJ, 162, 47
Bouwens R. J., Illingworth G. D., Franx M., Ford H., 2008, ApJ, 686, 230
Bouwens R. J., Illingworth G. D., Oesch P. A., Caruana J., Holwerda B., Smit R., Wilkins S., 2015, ApJ, 811, 140
Boylan-Kolchin M., 2023, Nat. Astron., 963, 128
Bradley L. et al., 2022, astropy/photutils: 1.5.0, https://doi.org/10.5281/zenodo.6825092
Brammer G. B., van Dokkum P. G., Coppi P., 2008, ApJ, 686, 1503
Brammer G., , 2018, gbrammer/grizli: Preliminary release, Zenodo
Bruzual G., Charlot S., 2003, MNRAS, 344, 1000
Calzetti D., Armus L., Bohlin R. C., Kinney A. L., Koornneef J., Storchi-Bergmann T., 2000, ApJ, 533, 682
Caputi K. I. et al., 2012, ApJ, 750, L20
Caputi K. I. et al., 2015, ApJ, 810, 73
Cardelli J. A., Clayton G. C., Mathis J. S., 1989, ApJ, 345, 245
Carnall A. C. et al., 2023, Nature, 619, 716
Carnall A. C., McLure R. J., Dunlop J. S., Davé R., 2018, MNRAS, 480, 4379
Carrasco D., Trenti M., Mutch S., Oesch P. A., 2018, PASA, 35, e022
Casey C. M. et al., 2023, ApJ, 954, 31
Chabrier G., 2003, PASP, 115, 763
Charlot S., Fall S. M., 2000, ApJ, 539, 718
Ciesla L., Elbaz D., Fensch J., 2017, A&A, 608, A41
Davidzon I. et al., 2017, A&A, 605, A70
Dekel A., Sarkar K. C., Birnboim Y., Mandelker N., Li Z., 2023, MNRAS, 523, 3201
Dickinson M., Papovich C., Ferguson H. C., Budavári T., 2003, ApJ, 587, 25
Dudzevičiūtė U. et al., 2020, MNRAS, 494, 3828
Faisst A. L. et al., 2020, ApJS, 247, 61
Finkelstein S. L. et al., 2015, ApJ, 814, 95
Finkelstein S. L. et al., 2022, ApJ, 940, L55
Finkelstein S. L. et al., 2023, ApJ, 946, L13
Fitzpatrick E. L., Massa D., 2007, ApJ, 663, 320
Franco M. et al., 2018, A&A, 620, A152
Fudamoto Y. et al., 2021, Nature, 597, 489
Gardner J. P. et al., 2023, PASP, 135, 068001
Gehrels N., 1986, ApJ, 303, 336
Gómez-Guijarro C. et al., 2023, A&A, 677, A34
González V., Labbé I., Bouwens R. J., Illingworth G., Franx M., Kriek M., Brammer G. B., 2010, ApJ, 713, 115
Gould K. M. L. et al., 2023, AJ, 165, 248
Greene J. E. et al., 2024, ApJ 964 39
Grogin N. A. et al., 2011, ApJS, 197, 35
Häußler B. et al., 2013, MNRAS, 430, 330
Huang J. S., Zheng X. Z., Rigopoulou D., Magdis G., Fazio G. G., Wang T., 2011, ApJ, 742, L13
Hunter J. D., 2007, Comput. Sci. Eng., 9, 90
Kluyver T. et al., 2016, in Loizides F., Schmidt B.eds, IOS Press BV, 87, 1013 BG Amsterdam Netherlands
Kocevski D. D. et al., 2023, ApJ, 954, L4
Koekemoer A. M. et al., 2011, ApJS, 197, 36
Kroupa P., 2001, MNRAS, 322, 231
Labbé I. et al., 2013, ApJ, 777, L19
Labbe I. et al., 2023a, preprint (arXiv:2306.07320)
Labbé I. et al., 2023b, Nature, 616, 266

Leethochawalit N., Trenti M., Morishita T., Roberts-Borsani G., Treu T., 2022, MNRAS, 509, 5836
Long A. S. et al., 2023a, preprint (arXiv:2305.04662)
Long A. S., Casey C. M., del P. Lagos C., Lambrides E. L., Zavala J. A., Champagne J., Cooper O. R., Cooray A. R., 2023b, ApJ, 953, 11
Madau P., Dickinson M., 2014, ARA&A, 52, 415
Manning S. M. et al., 2022, ApJ, 925, 23
Mason C. A., Trenti M., Treu T., 2023, MNRAS, 521, 497
Matthee J. et al., 2023, preprint (arXiv:2306.05448)
Maxwell E. A., 2011, preprint (arXiv:1102.0822)
McLeod D. J., McLure R. J., Dunlop J. S., Cullen F., Carnall A. C., Duncan K., 2021, MNRAS, 503, 4413
Menci N., Castellano M., Santini P., Merlin E., Fontana A., Shankar F., 2022, ApJ, 938, L5
Naidu R. P. et al., 2022, preprint (arXiv:2208.02794)
Navarro-Carrera R. et al. 2024, ApJ, 961, 16
Nelson E. J. et al., 2023, ApJ, 948, L18
Oesch P. A. et al., 2016, ApJ, 819, 129
Oesch P. A. et al., 2023, MNRAS, 525, 2864
Oke J. B., Gunn J. E., 1983, ApJ, 266, 713
Oliphant T. E., 2015, Guide to NumPy. CreateSpace Independent Publishing Platform Scotts Valley, California, US
Perez F., Granger B. E., 2007, Comput. Sci. Eng., 9, 21
Pérez-González P. G. et al., 2023, ApJ, 946, L16
Planck CollaborationXIII, 2016, A&A, 594, A13
Pozzetti L. et al., 2010, A&A, 523, A13
Rieke M. J. et al., 2023, PASP, 135, 028001
Rodighiero G., Bisigello L., Iani E., Marasco A., Grazian A., Sinigaglia F., Cassata P., Gruppioni C., 2023, MNRAS, 518, L19
Salpeter E. E., 1955, ApJ, 121, 161
Santini P. et al., 2021, A&A, 652, A30
Schaerer D., de Barros S., Sklias P., 2013, A&A, 549, A4
Schechter P., 1976, ApJ, 203, 297
Schlafly E. F., Finkbeiner D. P., 2011, ApJ, 737, 103
Schmidt M., 1968, ApJ, 151, 393
Shu X. et al., 2022, ApJ, 926, 155
Simpson J. M. et al., 2014, ApJ, 788, 125
Smail I. et al., 2021, MNRAS, 502, 3426
Somerville R. S., Lee K., Ferguson H. C., Gardner J. P., Moustakas L. A., Giavalisco M., 2004, ApJ, 600, L171
Speagle J. S., Steinhardt C. L., Capak P. L., Silverman J. D., 2014, ApJS, 214, 15
Spitler L. R. et al., 2014, ApJ, 787, L36
Stark D. P., Ellis R. S., Bunker A., Bundy K., Targett T., Benson A., Lacy M., 2009, ApJ, 697, 1493
Stefanon M. et al., 2015, ApJ, 803, 11
Stefanon M. et al., 2017a, ApJS, 229, 32
Stefanon M., Bouwens R. J., Labbé I., Illingworth G. D., Gonzalez V., Oesch P. A., 2021, ApJ, 922, 29
Stefanon M., Bouwens R. J., Labbé I., Muzzin A., Marchesini D., Oesch P., Gonzalez V., 2017b, ApJ, 843, 36
Sun F. et al., 2021, ApJ, 922, 114
Toft S. et al., 2014, ApJ, 782, 68
Trenti M., Stiavelli M., 2008, ApJ, 676, 767
Valentino F. et al., 2020, ApJ, 889, 93
Valentino F. et al., 2023, ApJ, 947, 20
Vika M., Vulcani B., Bamford S. P., Häußler B., Rojas A. L., 2015, A&A, 577, A97
Virtanen P. et al., 2020, Nature Methods, 17, 261
Wang T. et al., 2016, ApJ, 816, 84
Wang T. et al., 2019, Nature, 572, 211
Weaver J. et al., 2023a, in American Astronomical Society Meeting Abstracts. American Astronomical Society DC 20006 USA. p. 353.03D
Weaver J. R. et al., 2023b, A&A, 677, A184
Weibel A. et al. 2024, preprint (arXiv:2403.08872)
Williams C. C. et al., 2019, ApJ, 884, 154
Williams C. C. et al., 2023, preprint (arXiv:2311.07483)
Williams R. J., Quadri R. F., Franx M., van Dokkum P., Labbé I., 2009, ApJ, 691, 1879
Xiao M. et al., 2023a, preprint (arXiv:2309.02492)
Xiao M. Y. et al., 2023b, A&A, 672, A18
Yamaguchi Y. et al., 2019, ApJ, 878, 73
Zavala J. A. et al., 2021, ApJ, 909, 165
Zavala J. A. et al., 2023, ApJ, 943, L9

APPENDIX A: AGN IDENTIFICATION AND EFFECT ON THE SMF

Given that our study focuses on star-forming galaxies, it is of importance to remove AGN from our sample. We identify and remove AGN candidates, the so-called LRDs as described in Section 2.4. Fig. A1 shows the postage stamps and SED of one such AGN candidate, galaxy 6583. This is a very compact source, as is characteristic of LRDs, with a red slope beyond 2 μm and a blue slope below this. As shown, BAGPIPES does not fit the short-wavelength end of the slope well, possibly because BAGPIPES cannot perform multicomponent SED-fitting and additionally does not contain AGN templates. This results in inaccurate photometric redshifts and derived physical properties of LRDs. Further, Fig. A2 shows the effect of LRDs on the SMF of our sample. While the SMF of the full sample overlaps neatly with the AGN-cleaned sample at $3 < z < 4$, the difference between SMFs is more pronounced at $4 < z < 6$ and differs the most at $6 < z < 8$. This highlights the importance of addressing the presence of LRDs in our sample, so as not to overestimate the SMFs and stellar mass density at high redshifts.

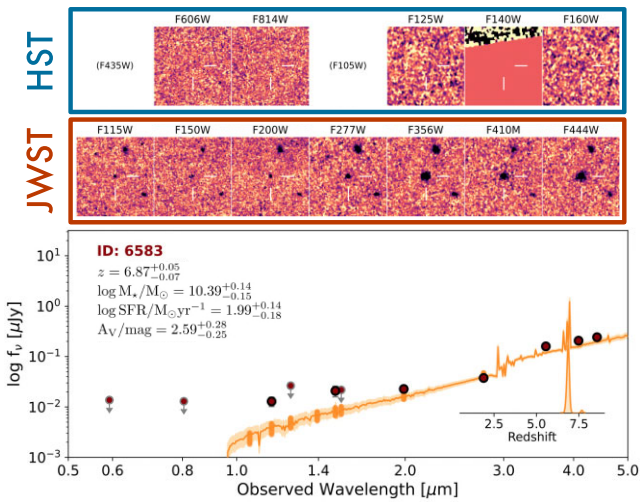

Figure A1. Postage stamps and SED of galaxy 6583, identified as a potential AGN and removed from our final sample. The postage stamps show the compactness of the source. The SED shows a characteristic red slope above 2 μm, and a blue slope below 2 μm. The blue part of the slope is poorly fit with BAGPIPES, thus resulting in an inaccurate photometric redshift and subsequently inaccurate derived physical properties.

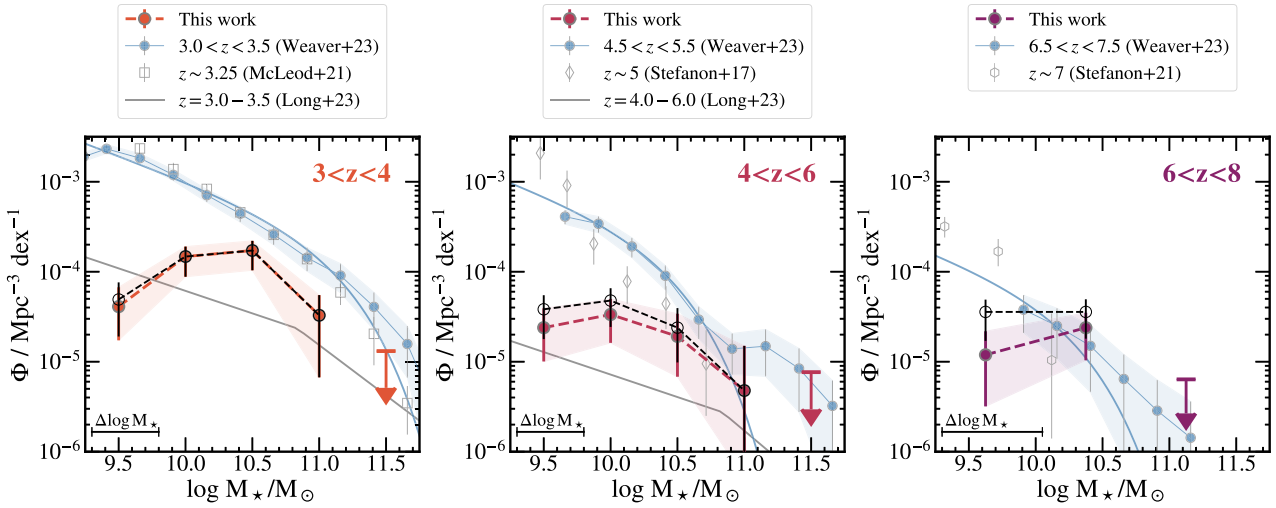

Figure A2. SMFs shown as in Fig. 8. In addition, open circles represent the SMFs of the full sample of 168 sources before AGN-removal. The AGN-removal has the least effect on the SMF at $3 < z < 4$, a larger effect at $4 < z < 6$ and the most pronounced effect at $6 < z < 8$. This highlights the importance of identifying and removing AGN candidates at high redshifts in order to derive accurate SMFs and SMD estimates.

APPENDIX B: PHYSICAL PROPERTIES OF GALAXIES FROM SED FITTING

Section 3 describes the SED-fitting performed with BAGPIPES. Here, we present the derived physical properties for the 168 galaxies in our sample: 148 star-forming galaxies and 20 AGN candidates. Table B1 presents the IDs, RA, Dec, photometric redshifts, stellar masses, SFRs, and dust attenuations of all galaxies. AGN candidates are indicated by a †.

Table B1. Physical properties of 168 red, optically faint galaxies in our sample. The 20 candidate AGN removed from the final sample are indicated by a †.

S. No.	ID	RA	Dec	$z_{\rm phot}$	log $M_\star/{\rm M}_\odot$	log SFR/$\rm M_\odot\ yr^{-1}$	$A_{\rm V}$ /mag
1†	2046	215.0817208	52.9122546	$7.76^{+0.30}_{-3.56}$	$9.79^{+0.19}_{-0.24}$	$1.51^{+0.22}_{-0.40}$	$2.53^{+1.22}_{-0.55}$
2	2090	215.0270820	52.8729121	$1.60^{+0.06}_{-0.03}$	$9.83^{+0.07}_{-0.09}$	$0.82^{+0.13}_{-0.13}$	$2.76^{+0.22}_{-0.19}$
3	2985	214.9892637	52.8471590	$0.99^{+0.07}_{-0.06}$	$10.00^{+0.08}_{-0.12}$	$-2.32^{+1.67}_{-3.47}$	$3.52^{+0.28}_{-0.33}$
4	3429	215.0884782	52.9187800	$2.01^{+0.26}_{-0.35}$	$9.94^{+0.15}_{-0.18}$	$1.08^{+0.25}_{-0.32}$	$3.33^{+0.30}_{-0.30}$
5†	3812	215.1370194	52.9556436	$8.46^{+0.30}_{-0.32}$	$9.98^{+0.21}_{-0.19}$	$2.00^{+0.20}_{-0.16}$	$2.82^{+0.37}_{-0.33}$
6	5145	215.1290424	52.9518497	$4.09^{+0.25}_{-0.37}$	$9.18^{+0.15}_{-0.30}$	$0.82^{+0.18}_{-0.40}$	$2.09^{+0.48}_{-0.31}$
7†	6583	214.8964766	52.7876910	$6.87^{+0.05}_{-0.07}$	$10.39^{+0.14}_{-0.15}$	$1.99^{+0.14}_{-0.18}$	$2.59^{+0.28}_{-0.25}$
8	6887	214.9056138	52.7912156	$2.86^{+0.09}_{-0.10}$	$11.32^{+0.06}_{-0.06}$	$2.55^{+0.11}_{-0.09}$	$3.87^{+0.09}_{-0.12}$
9	7125	215.0128418	52.8709202	$2.75^{+0.12}_{-0.18}$	$10.71^{+0.03}_{-0.05}$	$0.48^{+0.39}_{-0.63}$	$1.82^{+0.25}_{-0.27}$
10	7948	215.0804330	52.9215508	$3.02^{+0.47}_{-1.34}$	$10.28^{+0.12}_{-0.30}$	$1.60^{+0.19}_{-1.68}$	$3.11^{+0.50}_{-0.32}$
11	8099	214.9806159	52.8486131	$2.10^{+0.11}_{-0.11}$	$10.43^{+0.07}_{-0.11}$	$1.59^{+0.19}_{-0.12}$	$3.45^{+0.22}_{-0.22}$
12	8730	214.8544200	52.7595804	$1.92^{+0.08}_{-0.06}$	$10.31^{+0.05}_{-0.10}$	$1.40^{+0.16}_{-0.10}$	$3.12^{+0.20}_{-0.19}$
13	9030	215.0445212	52.8971830	$4.53^{+0.12}_{-0.14}$	$9.76^{+0.11}_{-0.08}$	$1.66^{+0.07}_{-0.13}$	$1.85^{+0.14}_{-0.16}$
14	9646	215.0759978	52.9213333	$4.81^{+0.10}_{-0.16}$	$9.86^{+0.06}_{-0.05}$	$1.29^{+0.09}_{-0.08}$	$1.60^{+0.12}_{-0.13}$
15	9823	214.8970451	52.7922215	$2.99^{+0.06}_{-0.08}$	$10.41^{+0.05}_{-0.11}$	$1.72^{+0.17}_{-0.10}$	$2.24^{+0.19}_{-0.14}$
16	10083	215.0348553	52.8913610	$2.70^{+0.11}_{-0.16}$	$11.06^{+0.05}_{-0.06}$	$2.26^{+0.12}_{-0.13}$	$3.79^{+0.14}_{-0.15}$
17	11399	214.9934658	52.8643256	$2.28^{+0.39}_{-0.11}$	$10.29^{+0.08}_{-0.10}$	$1.26^{+0.22}_{-0.61}$	$2.75^{+0.46}_{-0.54}$
18	12620	214.8645568	52.7742302	$4.13^{+0.18}_{-2.30}$	$9.33^{+0.09}_{-0.56}$	$0.82^{+0.15}_{-0.74}$	$2.10^{+0.94}_{-0.21}$
19	13192	214.9117928	52.8090634	$6.33^{+0.12}_{-0.11}$	$10.27^{+0.05}_{-0.05}$	$1.14^{+0.18}_{-0.16}$	$1.00^{+0.18}_{-0.16}$
20	13632	214.8998108	52.8015440	$8.90^{+0.76}_{-0.29}$	$9.83^{+0.29}_{-0.21}$	$1.61^{+0.31}_{-0.20}$	$1.93^{+0.31}_{-0.25}$
21	13789	215.1506541	52.9801120	$1.89^{+0.10}_{-0.07}$	$10.18^{+0.07}_{-0.09}$	$1.23^{+0.14}_{-0.14}$	$2.89^{+0.22}_{-0.17}$
22	14669	215.0722340	52.9253267	$5.23^{+0.06}_{-0.11}$	$10.28^{+0.09}_{-0.09}$	$2.12^{+0.06}_{-0.08}$	$2.15^{+0.10}_{-0.09}$

Table B1 – *continued*

S. No.	ID	RA	Dec	$z_{\rm phot}$	log $M_\star/{\rm M}_\odot$	log SFR/${\rm M}_\odot\,{\rm yr}^{-1}$	$A_{\rm V}$ /mag
23†	14807	214.9551930	52.8430203	$5.37^{+0.04}_{-0.03}$	$9.71^{+0.13}_{-0.11}$	$1.72^{+0.06}_{-0.07}$	$2.20^{+0.10}_{-0.11}$
24†	15203	214.9349717	52.8293673	$5.97^{+0.31}_{-0.18}$	$9.23^{+0.14}_{-0.10}$	$1.25^{+0.09}_{-0.10}$	$2.05^{+0.19}_{-0.22}$
25	15328	214.9799606	52.8610729	$6.94^{+0.12}_{-0.06}$	$10.17^{+0.04}_{-0.05}$	$1.26^{+0.08}_{-0.06}$	$0.52^{+0.09}_{-0.05}$
26	15607	214.9711828	52.8548811	$3.03^{+0.03}_{-0.03}$	$9.93^{+0.03}_{-0.02}$	$2.02^{+0.02}_{-0.02}$	$2.85^{+0.04}_{-0.05}$
27	15791	214.9438346	52.8358144	$5.44^{+0.05}_{-0.06}$	$10.52^{+0.08}_{-0.09}$	$2.08^{+0.09}_{-0.08}$	$2.32^{+0.12}_{-0.10}$
28	15973	214.9831267	52.8639966	$2.74^{+0.07}_{-0.09}$	$10.36^{+0.06}_{-0.08}$	$1.62^{+0.12}_{-0.13}$	$2.23^{+0.16}_{-0.13}$
29	16514	214.8097475	52.7396845	$2.19^{+0.17}_{-0.12}$	$10.27^{+0.10}_{-0.12}$	$1.34^{+0.15}_{-0.23}$	$3.30^{+0.27}_{-0.44}$
30	18000	214.8540675	52.7735451	$3.14^{+0.16}_{-0.48}$	$10.23^{+0.10}_{-0.32}$	$1.66^{+0.12}_{-0.14}$	$2.22^{+0.50}_{-0.24}$
31	18027	214.8528902	52.7739402	$3.91^{+0.15}_{-0.11}$	$10.29^{+0.06}_{-0.12}$	$1.73^{+0.14}_{-0.12}$	$2.00^{+0.19}_{-0.16}$
32	18652	214.8250625	52.7557775	$3.24^{+0.37}_{-0.45}$	$8.79^{+0.08}_{-0.15}$	$0.07^{+0.14}_{-0.20}$	$1.41^{+0.35}_{-0.18}$
33	19364	214.8906538	52.8030515	$5.13^{+0.13}_{-1.42}$	$11.04^{+0.10}_{-0.33}$	$2.56^{+0.09}_{-0.61}$	$3.84^{+0.13}_{-0.19}$
34	19829	214.8829253	52.7981532	$3.47^{+0.09}_{-0.13}$	$10.56^{+0.07}_{-0.10}$	$1.92^{+0.12}_{-0.10}$	$3.77^{+0.15}_{-0.17}$
35	20407	214.9966641	52.8805028	$2.33^{+0.03}_{-0.03}$	$9.88^{+0.15}_{-0.12}$	$1.80^{+0.04}_{-0.08}$	$3.13^{+0.12}_{-0.16}$
36†	21236	214.8997094	52.8128429	$5.46^{+1.53}_{-0.05}$	$9.80^{+0.29}_{-0.17}$	$1.75^{+0.11}_{-0.08}$	$2.48^{+0.17}_{-0.48}$
37	21274	214.9613710	52.8574003	$5.18^{+0.05}_{-0.06}$	$9.71^{+0.09}_{-0.10}$	$1.70^{+0.06}_{-0.05}$	$2.56^{+0.16}_{-0.15}$
38	21534	215.0413182	52.9140811	$2.14^{+0.53}_{-0.30}$	$10.75^{+0.10}_{-0.09}$	$1.68^{+0.32}_{-1.80}$	$3.45^{+0.40}_{-0.25}$
39	21642	214.8191823	52.7553065	$3.81^{+0.11}_{-1.21}$	$9.65^{+0.19}_{-0.21}$	$1.50^{+0.08}_{-0.36}$	$1.98^{+0.22}_{-0.20}$
40†	23057	214.8945658	52.8121655	$5.77^{+0.23}_{-0.18}$	$10.30^{+0.12}_{-0.18}$	$2.00^{+0.14}_{-0.16}$	$3.02^{+0.29}_{-0.24}$
41	24455	214.9331814	52.8415583	$3.49^{+0.07}_{-0.29}$	$9.74^{+0.09}_{-0.11}$	$1.22^{+0.14}_{-0.15}$	$1.61^{+0.19}_{-0.14}$
42	24824	215.1370832	52.9885559	$7.31^{+0.06}_{-0.05}$	$9.64^{+0.07}_{-0.06}$	$1.72^{+0.06}_{-0.05}$	$1.90^{+0.10}_{-0.09}$
43	24835	214.9076300	52.8234531	$3.56^{+0.09}_{-0.07}$	$10.50^{+0.09}_{-0.14}$	$1.97^{+0.13}_{-0.12}$	$3.85^{+0.11}_{-0.16}$
44	25691	215.0154584	52.9009634	$3.60^{+0.05}_{-0.05}$	$10.16^{+0.05}_{-0.04}$	$2.23^{+0.03}_{-0.04}$	$2.63^{+0.06}_{-0.06}$
45	25864	214.9967509	52.8890337	$3.59^{+0.07}_{-0.06}$	$10.29^{+0.11}_{-0.09}$	$2.27^{+0.04}_{-0.04}$	$2.73^{+0.09}_{-0.10}$
46	25923	215.1357255	52.9875677	$1.49^{+0.06}_{-0.08}$	$9.88^{+0.09}_{-0.12}$	$0.94^{+0.14}_{-0.12}$	$3.05^{+0.27}_{-0.23}$
47	26371	214.8748937	52.8014448	$2.85^{+0.08}_{-0.08}$	$10.27^{+0.06}_{-0.12}$	$1.50^{+0.17}_{-0.09}$	$1.78^{+0.22}_{-0.10}$
48	27302	214.8949216	52.8171584	$3.01^{+0.05}_{-0.07}$	$10.45^{+0.10}_{-0.19}$	$1.92^{+0.21}_{-0.18}$	$2.92^{+0.26}_{-0.20}$
49†	27673	214.8760429	52.8061119	$7.86^{+0.06}_{-0.06}$	$9.90^{+0.07}_{-0.08}$	$1.61^{+0.10}_{-0.07}$	$1.47^{+0.15}_{-0.11}$
50	27813	215.0312932	52.9171046	$3.47^{+0.07}_{-0.09}$	$10.29^{+0.10}_{-0.13}$	$1.85^{+0.12}_{-0.12}$	$3.79^{+0.14}_{-0.22}$
51	28768	214.9813321	52.8825635	$4.42^{+0.12}_{-0.12}$	$10.28^{+0.07}_{-0.09}$	$1.88^{+0.13}_{-0.14}$	$2.18^{+0.16}_{-0.16}$
52	29661	214.8607038	52.7968401	$3.04^{+0.15}_{-0.05}$	$10.85^{+0.07}_{-0.09}$	$2.15^{+0.14}_{-0.11}$	$3.50^{+0.22}_{-0.19}$
53	29799	214.7833571	52.7418112	$3.58^{+0.07}_{-0.05}$	$9.61^{+0.08}_{-0.06}$	$1.63^{+0.04}_{-0.04}$	$1.79^{+0.05}_{-0.08}$
54	29820	214.9623604	52.8700379	$3.29^{+0.28}_{-0.34}$	$10.42^{+0.23}_{-0.16}$	$2.19^{+0.12}_{-0.19}$	$3.52^{+0.21}_{-0.23}$
55	30392	214.8125539	52.7627779	$2.70^{+1.09}_{-0.18}$	$9.77^{+0.19}_{-0.15}$	$1.08^{+0.29}_{-0.17}$	$1.95^{+0.26}_{-0.27}$
56	30545	214.8852115	52.8157469	$2.84^{+0.23}_{-0.16}$	$10.51^{+0.15}_{-0.18}$	$2.14^{+0.10}_{-0.18}$	$3.52^{+0.23}_{-0.27}$
57	31590	215.0110259	52.9080516	$3.37^{+0.07}_{-0.08}$	$10.21^{+0.05}_{-0.07}$	$1.54^{+0.11}_{-0.09}$	$1.67^{+0.13}_{-0.10}$
58	32459	214.8327532	52.7813617	$3.73^{+0.35}_{-0.11}$	$10.25^{+0.14}_{-0.18}$	$1.82^{+0.13}_{-0.17}$	$3.67^{+0.21}_{-0.26}$
59	33202	214.8052770	52.7628116	$3.07^{+0.78}_{-0.52}$	$9.89^{+0.20}_{-0.32}$	$1.44^{+0.27}_{-0.27}$	$2.40^{+0.40}_{-0.29}$
60	33383	214.7737355	52.7403918	$1.00^{+0.12}_{-0.09}$	$8.41^{+0.19}_{-0.17}$	$-0.68^{+0.24}_{-0.23}$	$3.43^{+0.36}_{-0.66}$
61†	33394	214.9241508	52.8490510	$4.83^{+0.05}_{-0.04}$	$10.22^{+0.06}_{-0.06}$	$1.57^{+0.08}_{-0.29}$	$1.78^{+0.11}_{-0.38}$
62	33621	214.7739154	52.7413502	$8.04^{+0.41}_{-0.31}$	$9.80^{+0.10}_{-0.19}$	$1.57^{+0.10}_{-0.14}$	$1.68^{+0.18}_{-0.15}$
63	34437	214.7738211	52.7400098	$3.50^{+0.07}_{-0.16}$	$10.58^{+0.06}_{-0.10}$	$1.96^{+0.13}_{-0.11}$	$2.22^{+0.17}_{-0.12}$
64	35262	214.8464660	52.7959697	$1.86^{+0.34}_{-0.28}$	$9.88^{+0.17}_{-0.16}$	$0.88^{+0.36}_{-0.27}$	$3.54^{+0.28}_{-0.39}$
65†	35580	214.8501142	52.8000522	$4.10^{+0.37}_{-2.53}$	$9.27^{+0.10}_{-0.75}$	$0.64^{+0.17}_{-0.92}$	$1.62^{+1.14}_{-0.22}$
66	36882	214.8426487	52.7954529	$1.55^{+0.07}_{-0.09}$	$9.78^{+0.09}_{-0.12}$	$0.83^{+0.18}_{-0.12}$	$3.14^{+0.32}_{-0.26}$
67	39594	214.7713801	52.7497509	$3.63^{+0.09}_{-0.09}$	$10.64^{+0.08}_{-0.06}$	$1.91^{+0.09}_{-0.82}$	$3.85^{+0.11}_{-0.44}$
68	40635	214.8182953	52.7863215	$1.84^{+0.14}_{-0.19}$	$10.07^{+0.10}_{-0.11}$	$1.10^{+0.21}_{-0.21}$	$3.67^{+0.22}_{-0.25}$
69	40641	214.8402710	52.8011104	$6.19^{+0.24}_{-0.28}$	$10.47^{+0.11}_{-0.12}$	$2.30^{+0.10}_{-0.11}$	$1.87^{+0.13}_{-0.16}$
70	41002	214.8550845	52.8130408	$4.01^{+0.12}_{-0.10}$	$9.90^{+0.05}_{-0.07}$	$1.23^{+0.10}_{-0.07}$	$1.46^{+0.13}_{-0.09}$
71	41028	214.9415578	52.8742101	$2.90^{+0.11}_{-0.08}$	$10.22^{+0.11}_{-0.14}$	$1.75^{+0.12}_{-0.16}$	$1.91^{+0.17}_{-0.19}$
72	41343	214.7993284	52.7740023	$5.17^{+0.04}_{-0.05}$	$9.14^{+0.08}_{-0.08}$	$1.15^{+0.06}_{-0.05}$	$1.93^{+0.11}_{-0.13}$

Table B1 – *continued*

S. No.	ID	RA	Dec	$z_{\rm phot}$	log $M_\star/{\rm M}_\odot$	log SFR/${\rm M}_\odot\,{\rm yr}^{-1}$	$A_{\rm V}$ /mag
73	41769	214.8183966	52.7863542	$2.39^{+0.27}_{-0.27}$	$10.48^{+0.13}_{-0.13}$	$2.15^{+0.15}_{-0.22}$	$3.66^{+0.26}_{-0.22}$
74†	42428	214.8493875	52.8118246	$6.24^{+0.21}_{-0.19}$	$10.10^{+0.07}_{-0.08}$	$1.63^{+0.11}_{-0.09}$	$1.77^{+0.11}_{-0.11}$
75†	43895	214.9909773	52.9165225	$7.88^{+0.19}_{-1.98}$	$10.33^{+0.12}_{-0.12}$	$2.19^{+0.14}_{-0.21}$	$2.38^{+0.28}_{-0.23}$
76	44383	214.7610833	52.7506849	$3.80^{+0.06}_{-0.85}$	$10.13^{+0.12}_{-0.33}$	$1.79^{+0.14}_{-0.25}$	$1.77^{+0.22}_{-0.18}$
77	44999	214.8967047	52.8497952	$2.12^{+0.09}_{-0.08}$	$10.36^{+0.09}_{-0.14}$	$1.61^{+0.18}_{-0.17}$	$3.12^{+0.27}_{-0.26}$
78	45609	214.8871213	52.8453774	$3.65^{+0.25}_{-0.10}$	$9.46^{+0.10}_{-0.17}$	$0.93^{+0.12}_{-0.13}$	$1.80^{+0.18}_{-0.20}$
79	46100	214.8098740	52.7894326	$3.52^{+0.11}_{-0.32}$	$10.48^{+0.08}_{-0.15}$	$1.87^{+0.13}_{-0.13}$	$3.03^{+0.32}_{-0.18}$
80	48444	214.8405363	52.8179423	$8.14^{+0.23}_{-0.18}$	$9.65^{+0.18}_{-0.13}$	$1.67^{+0.14}_{-0.13}$	$2.10^{+0.25}_{-0.21}$
81	50438	214.7352152	52.7451418	$3.13^{+0.46}_{-0.26}$	$10.50^{+0.15}_{-0.13}$	$1.84^{+0.19}_{-0.19}$	$3.72^{+0.19}_{-0.27}$
82	50590	214.7338969	52.7444469	$2.15^{+0.29}_{-0.14}$	$10.24^{+0.12}_{-0.14}$	$1.50^{+0.17}_{-0.22}$	$3.08^{+0.24}_{-0.35}$
83	51072	214.9295156	52.8879151	$7.26^{+0.26}_{-0.17}$	$10.58^{+0.13}_{-0.14}$	$2.28^{+0.12}_{-0.14}$	$3.66^{+0.22}_{-0.25}$
84	51077	214.9785566	52.9215403	$2.51^{+0.08}_{-0.06}$	$10.44^{+0.04}_{-0.05}$	$-1.32^{+0.77}_{-1.27}$	$1.01^{+0.30}_{-0.17}$
85	51978	214.8706665	52.8461073	$3.58^{+0.09}_{-0.07}$	$10.10^{+0.14}_{-0.15}$	$1.72^{+0.14}_{-0.18}$	$2.56^{+0.21}_{-0.19}$
86	52049	214.7230124	52.7397625	$3.60^{+0.19}_{-0.11}$	$10.74^{+0.10}_{-0.09}$	$2.06^{+0.13}_{-0.10}$	$3.93^{+0.05}_{-0.14}$
87	52288	214.8403421	52.8249495	$2.29^{+0.07}_{-0.07}$	$10.68^{+0.05}_{-0.06}$	$1.81^{+0.11}_{-0.11}$	$3.61^{+0.19}_{-0.21}$
88	52954	214.7291876	52.7446890	$2.45^{+0.04}_{-0.05}$	$10.03^{+0.10}_{-0.11}$	$1.85^{+0.06}_{-0.09}$	$2.71^{+0.13}_{-0.10}$
89	53395	214.8624249	52.8429058	$2.88^{+0.26}_{-0.23}$	$10.21^{+0.18}_{-0.14}$	$2.06^{+0.11}_{-0.11}$	$3.19^{+0.20}_{-0.18}$
90	54147	214.8296607	52.8207741	$3.63^{+0.07}_{-0.06}$	$10.36^{+0.14}_{-0.12}$	$2.09^{+0.10}_{-0.15}$	$3.16^{+0.13}_{-0.17}$
91	55631	214.8099701	52.8097415	$3.68^{+0.31}_{-0.09}$	$10.78^{+0.27}_{-0.12}$	$2.70^{+0.06}_{-0.09}$	$3.73^{+0.11}_{-0.22}$
92	56217	214.9475951	52.9111224	$1.72^{+0.08}_{-0.08}$	$9.62^{+0.11}_{-0.10}$	$0.55^{+0.20}_{-0.78}$	$2.69^{+0.26}_{-0.60}$
93	56832	214.8769354	52.8603939	$2.68^{+0.12}_{-0.33}$	$10.62^{+0.08}_{-0.14}$	$1.88^{+0.18}_{-0.18}$	$3.13^{+0.27}_{-0.19}$
94	56856	214.9119355	52.8857565	$3.56^{+0.12}_{-0.05}$	$9.80^{+0.09}_{-0.08}$	$1.79^{+0.05}_{-0.04}$	$1.75^{+0.06}_{-0.08}$
95	57143	214.8719994	52.8593098	$7.33^{+0.14}_{-0.09}$	$8.77^{+0.15}_{-0.16}$	$0.76^{+0.13}_{-0.10}$	$1.16^{+0.22}_{-0.19}$
96	57734	214.7181000	52.7481020	$2.65^{+0.51}_{-0.15}$	$10.03^{+0.20}_{-0.19}$	$1.43^{+0.26}_{-0.17}$	$3.57^{+0.25}_{-0.38}$
97	57837	214.8348814	52.8323851	$2.45^{+0.12}_{-0.08}$	$10.21^{+0.10}_{-0.13}$	$1.63^{+0.10}_{-0.16}$	$2.27^{+0.19}_{-0.20}$
98	57866	214.9165099	52.8907640	$2.83^{+0.11}_{-0.12}$	$10.71^{+0.07}_{-0.10}$	$1.97^{+0.16}_{-0.13}$	$3.76^{+0.15}_{-0.17}$
99	58375	214.9135356	52.8910105	$4.01^{+0.36}_{-2.21}$	$9.21^{+0.21}_{-0.49}$	$0.84^{+0.23}_{-0.91}$	$2.07^{+0.77}_{-0.32}$
100	58801	214.7632325	52.7826809	$2.17^{+1.49}_{-0.40}$	$10.08^{+0.35}_{-0.20}$	$1.21^{+0.76}_{-0.35}$	$3.59^{+0.32}_{-0.79}$
101	59223	214.8922499	52.8774089	$7.28^{+0.15}_{-0.13}$	$10.65^{+0.04}_{-0.03}$	$1.68^{+0.07}_{-0.06}$	$1.24^{+0.09}_{-0.06}$
102	60533	214.8560303	52.8546725	$3.67^{+0.45}_{-0.32}$	$9.97^{+0.29}_{-0.18}$	$1.77^{+0.11}_{-0.39}$	$3.26^{+0.23}_{-0.43}$
103	60809	214.8557255	52.8546205	$3.10^{+0.18}_{-0.13}$	$9.50^{+0.07}_{-0.11}$	$0.79^{+0.13}_{-0.11}$	$1.78^{+0.22}_{-0.19}$
104	61017	214.8558862	52.8546713	$1.89^{+1.73}_{-0.22}$	$9.86^{+0.42}_{-0.14}$	$0.94^{+0.86}_{-0.26}$	$3.51^{+0.33}_{-0.91}$
105	61155	214.9050035	52.8903902	$3.57^{+0.11}_{-0.08}$	$10.03^{+0.17}_{-0.13}$	$1.83^{+0.08}_{-0.16}$	$2.97^{+0.15}_{-0.14}$
106	61732	214.9509311	52.9239597	$1.80^{+0.18}_{-0.34}$	$9.94^{+0.14}_{-0.15}$	$1.05^{+0.23}_{-0.24}$	$3.30^{+0.34}_{-0.28}$
107	62882	214.7581773	52.7872067	$2.80^{+0.08}_{-0.07}$	$10.07^{+0.06}_{-0.10}$	$1.33^{+0.17}_{-0.13}$	$2.21^{+0.19}_{-0.16}$
108	63309	214.8476073	52.8534055	$4.19^{+0.42}_{-0.59}$	$9.84^{+0.15}_{-0.29}$	$1.35^{+0.20}_{-0.38}$	$3.28^{+0.31}_{-0.25}$
109	63467	214.8475506	52.8533680	$4.28^{+0.47}_{-0.39}$	$10.25^{+0.18}_{-0.16}$	$1.65^{+0.20}_{-0.19}$	$3.86^{+0.10}_{-0.19}$
110	63642	214.8588311	52.8603958	$1.96^{+0.52}_{-0.40}$	$10.02^{+0.21}_{-0.24}$	$1.17^{+0.27}_{-0.38}$	$3.34^{+0.40}_{-0.48}$
111	63912	214.9375051	52.9182908	$3.94^{+0.07}_{-0.07}$	$9.98^{+0.10}_{-0.11}$	$1.68^{+0.10}_{-0.20}$	$2.03^{+0.14}_{-0.18}$
112	64408	215.0229080	52.9800661	$3.58^{+0.07}_{-0.04}$	$9.90^{+0.10}_{-0.08}$	$1.90^{+0.04}_{-0.04}$	$2.17^{+0.07}_{-0.09}$
113	65999	214.7189003	52.7643900	$5.27^{+0.06}_{-0.22}$	$9.80^{+0.08}_{-0.09}$	$1.38^{+0.08}_{-0.08}$	$1.62^{+0.12}_{-0.11}$
114	66597	214.9254260	52.9133973	$2.31^{+0.08}_{-0.21}$	$9.94^{+0.11}_{-0.14}$	$1.23^{+0.16}_{-0.16}$	$2.48^{+0.23}_{-0.25}$
115	66608	214.8538962	52.8613647	$3.33^{+0.06}_{-0.09}$	$11.24^{+0.06}_{-0.13}$	$2.62^{+0.16}_{-0.11}$	$3.44^{+0.23}_{-0.15}$
116†	66755	214.6951558	52.7485691	$9.32^{+0.42}_{-0.51}$	$10.55^{+0.19}_{-0.25}$	$2.38^{+0.22}_{-0.29}$	$2.93^{+0.32}_{-0.28}$
117	66989	215.0368171	52.9935017	$1.82^{+0.09}_{-0.16}$	$9.82^{+0.07}_{-0.14}$	$0.86^{+0.21}_{-0.22}$	$2.67^{+0.23}_{-0.20}$
118	67066	214.9830245	52.9560011	$7.48^{+0.05}_{-0.04}$	$10.58^{+0.05}_{-0.05}$	$2.14^{+0.05}_{-0.05}$	$1.52^{+0.06}_{-0.06}$
119	67073	214.8001303	52.8232104	$2.80^{+0.12}_{-0.19}$	$10.31^{+0.08}_{-0.11}$	$1.42^{+0.22}_{-1.49}$	$1.79^{+0.23}_{-0.84}$
120	67919	214.9440410	52.9297441	$2.47^{+3.16}_{-0.08}$	$9.43^{+0.47}_{-0.20}$	$0.86^{+0.74}_{-0.24}$	$2.69^{+0.26}_{-0.76}$
121	68963	214.9315628	52.9210090	$2.49^{+0.22}_{-0.09}$	$9.89^{+0.15}_{-0.13}$	$1.14^{+0.20}_{-0.15}$	$3.71^{+0.19}_{-0.32}$
122†	69075	215.0084905	52.9779735	$7.96^{+0.07}_{-0.05}$	$9.45^{+0.06}_{-0.06}$	$1.53^{+0.06}_{-0.05}$	$1.47^{+0.10}_{-0.08}$

Table B1 – *continued*

S. No.	ID	RA	Dec	$z_{\rm phot}$	log $M_\star/{\rm M}_\odot$	log SFR/${\rm M}_\odot\,{\rm yr}^{-1}$	$A_{\rm V}$ /mag
123	69084	214.9774708	52.9534870	$3.76^{+0.09}_{-0.70}$	$10.94^{+0.14}_{-0.14}$	$2.43^{+0.21}_{-0.33}$	$3.72^{+0.20}_{-0.21}$
124	69557	214.9257560	52.9185250	$3.59^{+0.10}_{-0.15}$	$10.58^{+0.08}_{-0.13}$	$1.98^{+0.13}_{-0.14}$	$3.22^{+0.25}_{-0.16}$
125	69697	214.8890698	52.8926163	$3.60^{+0.09}_{-0.07}$	$10.63^{+0.09}_{-0.13}$	$2.12^{+0.15}_{-0.14}$	$3.32^{+0.17}_{-0.17}$
126	70195	214.8505690	52.8660278	$3.11^{+0.09}_{-0.09}$	$10.64^{+0.07}_{-0.17}$	$2.01^{+0.18}_{-0.14}$	$2.80^{+0.30}_{-0.21}$
127†	71049	214.8400344	52.8606505	$4.75^{+0.91}_{-0.15}$	$9.74^{+0.06}_{-0.09}$	$1.25^{+0.14}_{-0.12}$	$1.42^{+0.17}_{-0.12}$
128	71055	214.8790993	52.8880654	$3.02^{+0.02}_{-0.03}$	$9.85^{+0.16}_{-0.05}$	$1.89^{+0.03}_{-0.07}$	$2.36^{+0.06}_{-0.19}$
129	71122	215.0390567	53.0027819	$3.22^{+0.15}_{-0.12}$	$10.45^{+0.08}_{-0.07}$	$1.58^{+0.13}_{-0.58}$	$2.44^{+0.24}_{-0.65}$
130	72378	215.0215373	52.9913009	$2.70^{+1.71}_{-0.19}$	$10.95^{+0.42}_{-0.09}$	$2.17^{+0.95}_{-0.17}$	$3.90^{+0.07}_{-0.65}$
131	73426	214.8670444	52.8832805	$3.54^{+0.11}_{-0.34}$	$10.36^{+0.10}_{-0.10}$	$2.00^{+0.14}_{-0.21}$	$1.92^{+0.15}_{-0.17}$
132†	73685	214.9233729	52.9255931	$7.27^{+0.07}_{-0.07}$	$9.85^{+0.06}_{-0.05}$	$1.93^{+0.04}_{-0.05}$	$1.96^{+0.08}_{-0.06}$
133	73705	214.8013661	52.8370353	$3.64^{+0.05}_{-0.07}$	$9.80^{+0.09}_{-0.06}$	$1.85^{+0.04}_{-0.04}$	$2.30^{+0.06}_{-0.08}$
134	73825	215.0045564	52.9835262	$3.64^{+0.08}_{-0.08}$	$10.70^{+0.10}_{-0.15}$	$2.22^{+0.14}_{-0.12}$	$3.48^{+0.17}_{-0.18}$
135	74051	214.7856935	52.8258160	$2.07^{+0.37}_{-0.24}$	$10.22^{+0.15}_{-0.17}$	$1.72^{+0.23}_{-0.38}$	$3.39^{+0.20}_{-0.35}$
136†	74228	214.9724417	52.9621923	$7.24^{+0.14}_{-0.11}$	$9.86^{+0.11}_{-0.11}$	$1.64^{+0.14}_{-0.13}$	$1.98^{+0.21}_{-0.20}$
137	74393	214.8657827	52.8834206	$1.61^{+1.18}_{-0.21}$	$9.57^{+0.30}_{-0.15}$	$0.57^{+0.64}_{-0.21}$	$2.75^{+0.33}_{-0.50}$
138	75238	214.7680280	52.8163996	$3.59^{+0.09}_{-0.06}$	$10.54^{+0.10}_{-0.12}$	$2.03^{+0.15}_{-0.14}$	$3.49^{+0.21}_{-0.18}$
139	76999	214.7672283	52.8177106	$3.02^{+0.02}_{-0.02}$	$10.04^{+0.06}_{-0.03}$	$2.10^{+0.02}_{-0.02}$	$2.72^{+0.04}_{-0.07}$
140	77220	214.8396806	52.8717324	$2.96^{+0.12}_{-0.13}$	$9.73^{+0.06}_{-0.12}$	$1.03^{+0.16}_{-0.12}$	$1.79^{+0.22}_{-0.17}$
141	78330	214.7914982	52.8380321	$2.23^{+0.49}_{-0.14}$	$10.93^{+0.13}_{-0.08}$	$2.02^{+0.27}_{-0.16}$	$3.84^{+0.11}_{-0.33}$
142	79082	214.9183809	52.9378937	$2.80^{+0.18}_{-0.18}$	$9.89^{+0.08}_{-0.16}$	$1.20^{+0.19}_{-0.14}$	$2.14^{+0.26}_{-0.19}$
143	79446	214.8351098	52.8951289	$5.15^{+0.05}_{-0.05}$	$9.99^{+0.09}_{-0.08}$	$1.78^{+0.06}_{-0.08}$	$1.57^{+0.08}_{-0.11}$
144	79727	214.9257694	52.9544458	$2.06^{+1.74}_{-0.26}$	$9.63^{+0.41}_{-0.17}$	$0.78^{+0.65}_{-0.30}$	$3.49^{+0.35}_{-0.79}$
145	80544	215.0112724	53.0135961	$5.18^{+0.04}_{-0.04}$	$10.22^{+0.05}_{-0.05}$	$2.26^{+0.03}_{-0.03}$	$1.94^{+0.05}_{-0.04}$
146†	80697	214.7598250	52.8334125	$3.63^{+0.62}_{-1.97}$	$9.46^{+0.24}_{-0.56}$	$0.96^{+0.20}_{-1.00}$	$2.63^{+1.14}_{-0.39}$
147	81918	214.9145423	52.9430232	$4.79^{+0.05}_{-0.07}$	$9.12^{+0.09}_{-0.06}$	$1.08^{+0.05}_{-0.09}$	$1.74^{+0.11}_{-0.17}$
148	82924	214.9091113	52.9372134	$3.68^{+0.54}_{-0.39}$	$10.10^{+0.18}_{-0.16}$	$1.48^{+0.27}_{-0.23}$	$3.60^{+0.24}_{-0.26}$
149	83296	214.9040279	52.9327056	$2.10^{+0.44}_{-0.15}$	$10.53^{+0.10}_{-0.10}$	$1.61^{+0.20}_{-0.18}$	$3.48^{+0.25}_{-0.37}$
150†	83338	214.9508401	52.9668645	$3.83^{+0.34}_{-0.23}$	$9.64^{+0.11}_{-0.21}$	$1.11^{+0.14}_{-0.15}$	$2.36^{+0.27}_{-0.22}$
151	83822	214.7665808	52.8315226	$4.30^{+0.17}_{-0.13}$	$9.64^{+0.07}_{-0.10}$	$1.14^{+0.13}_{-0.11}$	$1.82^{+0.18}_{-0.15}$
152	83936	214.9491882	52.9641429	$6.20^{+0.20}_{-0.29}$	$9.46^{+0.09}_{-0.10}$	$1.52^{+0.08}_{-0.09}$	$2.09^{+0.13}_{-0.13}$
153†	84323	214.9257531	52.9456643	$7.27^{+0.11}_{-0.11}$	$9.83^{+0.12}_{-0.12}$	$1.84^{+0.11}_{-0.11}$	$2.48^{+0.19}_{-0.18}$
154	84655	214.8383963	52.8851887	$6.07^{+0.27}_{-0.23}$	$9.60^{+0.07}_{-0.07}$	$1.67^{+0.07}_{-0.06}$	$1.82^{+0.06}_{-0.07}$
155	85172	214.8109343	52.8589270	$3.01^{+0.31}_{-0.18}$	$9.62^{+0.09}_{-0.17}$	$0.90^{+0.17}_{-0.17}$	$1.90^{+0.30}_{-0.23}$
156	85249	214.9887041	52.9886234	$1.71^{+1.90}_{-0.11}$	$9.82^{+0.43}_{-0.14}$	$0.94^{+0.93}_{-0.22}$	$2.70^{+0.28}_{-0.73}$
157	85675	214.9469656	52.9602699	$1.95^{+0.18}_{-0.47}$	$10.01^{+0.14}_{-0.16}$	$1.24^{+0.27}_{-0.34}$	$2.66^{+0.29}_{-0.24}$
158	87151	214.8485472	52.8847626	$1.84^{+1.96}_{-0.19}$	$9.08^{+0.53}_{-0.15}$	$0.18^{+0.91}_{-0.21}$	$3.53^{+0.33}_{-1.03}$
159	87239	214.8111763	52.8586480	$2.18^{+1.49}_{-0.56}$	$10.33^{+0.14}_{-0.30}$	$1.78^{+0.69}_{-0.59}$	$3.34^{+0.45}_{-0.52}$
160	87370	214.7792320	52.8369189	$5.93^{+1.89}_{-2.17}$	$9.22^{+0.19}_{-0.46}$	$0.97^{+0.21}_{-0.61}$	$1.74^{+0.49}_{-0.36}$
161	87446	214.8751893	52.9134883	$2.96^{+0.08}_{-0.10}$	$10.01^{+0.09}_{-0.15}$	$1.46^{+0.15}_{-0.15}$	$2.07^{+0.20}_{-0.19}$
162	88423	214.8482919	52.8847861	$3.94^{+0.19}_{-2.14}$	$9.58^{+0.15}_{-0.46}$	$1.25^{+0.17}_{-0.93}$	$2.00^{+0.78}_{-0.23}$
163	88428	214.7634081	52.8477946	$1.77^{+0.11}_{-0.11}$	$10.14^{+0.09}_{-0.11}$	$1.10^{+0.16}_{-0.27}$	$3.74^{+0.17}_{-0.22}$
164	90408	214.8293099	52.8939285	$2.53^{+0.16}_{-0.32}$	$11.22^{+0.06}_{-0.07}$	$1.84^{+0.53}_{-1.21}$	$3.59^{+0.27}_{-0.53}$
165	90510	214.7437385	52.8368225	$3.78^{+0.04}_{-1.25}$	$10.58^{+0.09}_{-0.51}$	$2.62^{+0.04}_{-0.49}$	$2.69^{+0.28}_{-0.11}$
166	91433	214.8520783	52.9097650	$2.24^{+0.08}_{-0.09}$	$10.44^{+0.07}_{-0.10}$	$1.60^{+0.15}_{-0.11}$	$3.01^{+0.27}_{-0.23}$
167	92377	214.8918896	52.9338667	$3.96^{+1.78}_{-0.19}$	$10.36^{+0.27}_{-0.23}$	$1.93^{+0.39}_{-0.23}$	$3.10^{+0.35}_{-0.46}$
168	93595	214.9578855	52.9802999	$3.03^{+0.02}_{-0.02}$	$10.02^{+0.07}_{-0.03}$	$2.07^{+0.02}_{-0.02}$	$2.48^{+0.04}_{-0.06}$

This paper has been typeset from a TEX/LATEX file prepared by the author.